ROYAL SOCIETY OF CHEMISTRY

COMMUNICATION

Check for updates

The paradox of gold–liposome nanohybrids: the location of gold governs unconventional properties and drives cellular behavior

Ansuja P. Mathew,†[ab] Vandhana Kandavelkumar,†[ab] Nabila Masud,[c]
Sebastian Huerta-Romo Picazo,[d] Susheel Kumar Nethi,[ab] Saji Uthaman, [iD] ‡[ab]
Xiaona Wen,[b] Wenyu Huang, [iD] [d] Surya K. Mallapragada,[ab] Anwesha Sarkar[c] and
Rizia Bardhan [iD] *[ab]

The physicochemical characteristics of nanoparticles (NPs) and the cell type they encounter impact cellular interactions. Yet, which parameters should be precisely controlled to direct endocytosis in specific cell types remains paradoxical. Here, we designed gold–liposome nanohybrids (GLNs) and demonstrated for the first time that the location of gold either inside, outside, or partially in/out of the liposomes enables simultaneous tunability of their physical, molecular, mechanical, and optical properties that go beyond the conventional paradigm of size, shape, and charge. Well-controlled chitosan layers on the liposomes allowed the modulation of the position of gold, generating three distinct GLNs of similar size but varied topology (smooth to uneven to textured), surface molecular composition (lipid-rich to inorganic gold), stiffness (4 to 50.5 MPa), tunable resonances (visible to near-infrared) and photothermal conversion efficiency. These collective properties of GLNs governed cellular interactions in two distinct cell types, dendritic cells (DC2.4) and epithelial cells (MODE-K). Our findings show that (i) endocytosis is cell-type dependent and temporally-controlled varying significantly for the three GLNs, (ii) cells show sensitivity to the endocytosis rate even within the narrow stiffness range studied here, and (iii) the properties of GLNs control their therapeutic function from photothermal heating or mild hyperthermia in MODE-K to optically-driven immunostimulation in DC2.4. Our findings may ultimately establish new mechanisms of NP–cell interactions enabling the development of a family of novel NPs with unexplored properties applicable for a range of biomedical applications.

New concepts

In this work, gold–liposome nanohybrids (GLNs) were designed, where the location of gold on the liposomes, *i.e.* inside, outside, or partially in/out, was precisely controlled. This precision allowed us to tune the physical (topology), molecular (surface moieties), mechanical (stiffness) and optical (photothermal) properties simultaneously. These properties of nanoparticles (NPs) are mutually dependent and concurrently contribute to cell-specific interactions. However, the interplay of these critical parameters in modulating endocytosis has remained paradoxical thus far. Here we show that these properties of GLNs, which are hybrid NPs, collectively control (i) the kinetics of uptake in cells, which is both cell-type dependent and temporally-controlled, (ii) the endocytosis pathways they leverage to enter cells, which goes beyond the conventional pathways gold NPs or liposomes use, and (iii) the distinct therapeutic function they achieve in dendritic cells *vs.* intestinal epithelial cells. The fundamental underpinnings of this work will ultimately enable the establishment of new mechanisms that break existing paradigms to design novel hybrid NPs with unique properties and direct stimuli-controlled functions for different biomedical applications in the future.

Introduction

Cellular uptake of nanoparticles (NPs) and their transport through biological barriers are well-studied as a function of their size, shape, charge, and ligands.[1–3] Furthermore, NP accumulation in cells is also driven by the type and phenotype of the cells they encounter.[4] Despite these advances, which parameters of NPs should be modulated to direct their uptake in the target cells remains paradoxical. Thoughtfully designed NPs that leverage multiple physicochemical properties are imperative to enable spatiotemporally-controlled endocytosis in cells and achieve desired therapeutic function.[5] Here we synthesized gold–liposome nanohybrids (GLNs), where the location of gold on the liposomes, *i.e.* inside, outside, or partially in/out, was precisely controlled. Although gold–liposome NPs[6–9] have been well-studied for various therapeutic applications, our approach for designing GLNs brings an innovative direction. We highlight for the first time that the

a Department of Chemical and Biological Engineering, Iowa State University, Ames, Iowa, USA. E-mail: rbardhan@iastate.edu

b Nanovaccine Institute, Iowa State University, Ames, Iowa, USA

c Department of Electrical and Computer Engineering, Iowa State University, Ames, Iowa, USA

d Department of Chemistry, Iowa State University, Ames, Iowa, USA

† These authors have contributed equally.

‡ Current address: Smart Materials and Devices (SMAD) Division, Yenepoya Research Centre, Yenepoya (Deemed to be University), Mangalore, 575018, India.

location of gold on liposomes allows tuning the physical (topology), molecular (surface moieties), mechanical (stiffness) and optical (photothermal) properties simultaneously. These properties collectively enable cell-specific uptake, the kinetics of internalization, the endocytosis pathways they leverage to enter cells, and the therapeutic function. Prior works on gold–liposome NPs have focused on the binding of AuNPs on the outer surface of the liposomes or embedding them randomly into the lipid bilayer or loading of AuNPs within the liposomes. While such approaches may have achieved a therapeutic outcome, uncontrolled spatial distribution of Au limits tunability of their physicochemical properties as well as poses challenges with reproducibility.[10–12] Our approach enables spatial control of the placement of AuNPs on the liposomes, allowing tunability of unconventional properties of the resulting GLNs, which has not been studied previously. Furthermore, we chose to use AuNPs over other metals due to their established biocompatibility, low cytotoxicity, and chemical inertness that

is well suited for cellular interactions. AuNPs offer versatility in surface functionalization allowing spatial control of their placement on liposomes. AuNPs also facilitate tunability of their localized surface plasmon resonance (LSPR) into the near-infrared (NIR) to control their photothermal behavior that can be leveraged for therapeutic outcome.

When NPs encounter a cell, the surface moieties of NPs modulate cellular signals (Scheme 1); cells then respond to these cues and recognize the topology and stiffness of NPs.[13] NPs are wrapped in the cell membrane and endocytosed into endosomal vesicles that bud off the membrane. NPs with high stiffness, *i.e.* hard NPs, get fully wrapped in the membrane and internalized rapidly, while soft NPs undergo deformation and are trapped within the cell membrane and may impede endocytosis.[14,15] However, the rate of endocytosis is often dominated by receptor-diffusion controlled by surface ligands that can drive rapid internalization of even soft NPs.[16] Furthermore, the topology of both gold-based and lipid-based NPs
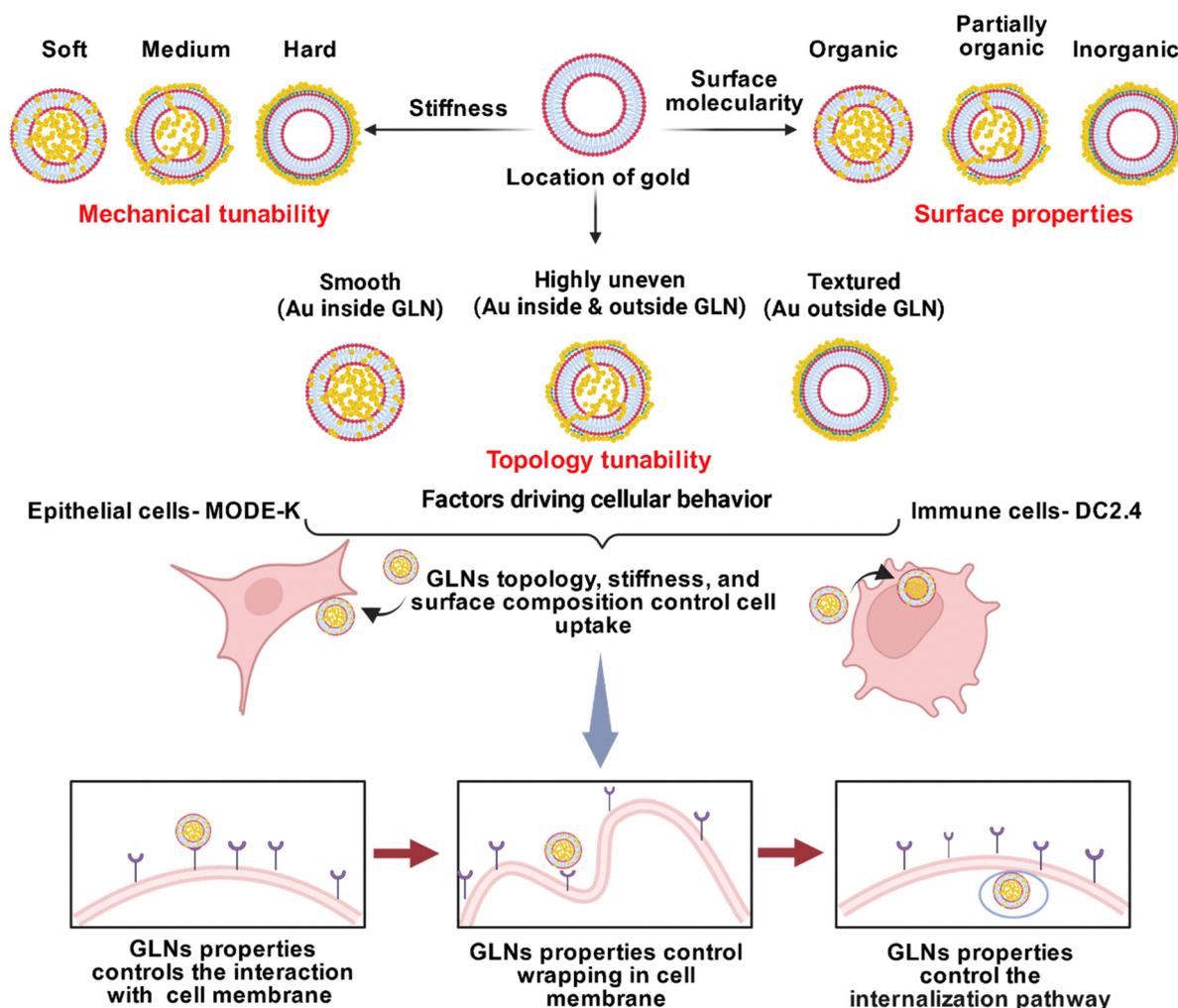
Scheme 1 Schematic illustration showing gold–liposome nanohybrids (GLNs) to achieve cell-specific uptake through mechanical (stiffness), molecular (surface ligands), and topological tunability, where the location of gold inside, outside, or partially inside/outside the liposomes governs these properties. These characteristics also drive the endocytosis pathways GLNs leverage to enter different cell-types. Illustration is created using the Biorender scientific illustration platform.

can regulate targeting efficiency and endosomal escape.[17,18] Indeed, NP topology and stiffness collectively dictate the degree of membrane wrapping and cytoskeletal engagement, while surface composition modulates receptor interactions and interfacial energy.[19] The initial rate of endocytosis of NPs is determined by the topology where a smooth surface could result in slower uptake, whereas an uneven surface that increases the overall surface area available to cells may enhance cellular interactions and promote faster internalization.[20] This process is also highly temporally controlled, *i.e.* initial *vs.* later phases of endocytosis, as well as cell-type dependent, where antigen-presenting cells such as dendritic cells (DCs) readily uptake stiffer NPs while epithelial cells prefer softer NPs with smoother surfaces. While these traditional mechanisms may hold true for solid AuNPs or liposomes, hybrid NPs such as GLNs elicit a distinct response where physical, molecular, and mechanical characteristics are synergistically aligned to enable appropriate membrane deformation and cellular internalization. This implies that these properties of NPs are mutually dependent and concurrently contribute to cell-specific endocytosis. Yet the interplay of these critical parameters and how they contribute to cellular interactions remain underexplored. These properties of NPs also impact the endocytosis pathways they utilize to enter cells and their ultimate fate *in vivo* such as targeting specific organs and clearance.[4] The classical endocytosis pathways NPs use include macropinocytosis, clathrin-mediated endocytosis (CLME), caveolae-mediated endocytosis (CavE), and phagocytosis.[4] Hard NPs are internalized through CLME, CavE, and macropinocytosis, while soft NPs are internalized *via* CavE and non-receptor mediated endocytosis.[21] In addition, surface properties of nanoparticles, including ligand type and ligand mobility, play a critical role in initiating endocytosis, primarily through clathrin-mediated endocytosis (CLME).[22,23] Furthermore, the cell-type and phenotype also influence these endocytosis pathways.[24,25] For example, epithelial cells primarily use CLME while macrophages/dendritic cells use phagocytosis and macropinocytosis to internalize NPs.[26]

In this study, GLNs integrate "stiffer" gold NPs and "softer" liposomes. Our findings show that GLNs with gold inside liposomes have a smooth topology, lipid-rich surface moieties, a low Young's modulus, and near-infrared (NIR) localized surface plasmon resonance (LSPR) that enables efficient photothermal conversion. GLNs with gold partially inside/out have a highly uneven topology, a mix of surface moieties including lipids and AuNPs, a medium Young's modulus and NIR LSPR with high photothermal efficiency. Finally, GLNs with gold completely outside forming a shell on liposomes have a textured topology, inorganic Au surface composition, and a high Young's modulus but LSPR in the visible region and weaker photothermal conversion. These properties enable distinct trends in uptake and endocytosis pathways in DC2.4 dendritic cells and MODE-K epithelial cells. Our findings will provide a roadmap for new hybrid NPs with tunable physicochemical properties targeted to elicit specific cellular responses.

Results and discussion

The location of gold on liposomes was precisely controlled through multiple chemical approaches such that the resulting GLNs have <200 nm sizes, tunable LSPR in the NIR for successful photothermal conversion, and desirable stiffness. We hypothesized that these properties of GLNs would then drive novel and unexpected cellular interactions. A number of synthesis techniques were used to synthesize GLNs inspired by well-established methods in the literature.[27,28] Our first approach leveraged the Au–S covalent bonds (Fig. 1a), where liposomes composed of thiol-terminated DSPE–PEG–SH lipids were first incubated with $HAuCl_4$ solution, where the Au^{3+} ions bind to the thiol (–SH) groups on liposomes and subsequently serve as nucleation sites for further AuNP growth. After this step, the liposomes + $HAuCl_4$ were coated with preformed Au seeds, where the covalent attachment of these Au seeds to liposomes catalyzes the reduction of gold ions *via* a seed-mediated growth approach, enabling the formation of a gold layer on the liposomes. Two different volume ratios of liposomes to gold seeds were examined, 1:1 and 1:2, to tune their size and LSPR. The extinction spectra of these two ratios showed LSPR at 550 nm that was not tunable beyond that range (Fig. 1b). This indicates that this approach likely did not grow a continuous gold shell and instead clusters of AuNPs were formed in the solution or bound to the liposomes. The hydrodynamic size of the liposomes incubated with $HAuCl_4$ was 240.8 ± 20.2 nm, and the sizes of the liposomes:gold seeds at ratios 1:1 and 1:2 were 258.8 ± 30 nm and 479.56 ± 54.86 nm, respectively (Fig. 1c). The observed increase in hydrodynamic size resulted from the aggregation of AuNPs, suggesting that this approach did not yield the desired morphology or size range. The average surface charge of the liposomes incubated with $HAuCl_4$ was 10.2 ± 1.2 mV, and that for liposomes:gold seeds at ratios 1:1 and 1:2 was 10.2 ± 3.4 mV, and 9.5 ± 2.1 mV, respectively (Fig. S1d). The nearly identical surface charge among the three samples indicates the lack of uniform gold growth on the liposomes. Transmission electron micrographs showed small islands of AuNPs surrounding liposomes and lack of a complete gold shell or gold inside (Fig. 1e), which corroborates with the trends in the extinction spectra and surface charge.

In our second approach, we pursued the direct reduction of AuNPs on liposomes composed of amine terminated DSPE–PEG–NH_2 lipids (Fig. 1f) with ascorbic acid as a reducing agent.[29,30] Our rationale was that strong covalent bonds of Au–NH_2 will allow Au^{3+} ions to attach to the liposome surface and ascorbic acid mediated conversion of Au^{3+} ions to Au^0 will facilitate nucleation and growth of the gold shell on the liposome. The ratio of ascorbic acid:$HAuCl_4$ was varied and we found that 6:1 and 8:1 ratios allowed tuning the LSPR to 600–700 nm (Fig. 1g) and achieved a desired hydrodynamic size of 170 ± 10 nm for the 6:1 ratio and 145 ± 5 nm for the 8:1 ratio (Fig. 1h). The surface charge also changed after gold reduction on liposomes where the positive charge of uncoated liposomes, 13 ± 2 mV, attributed to the positively charged
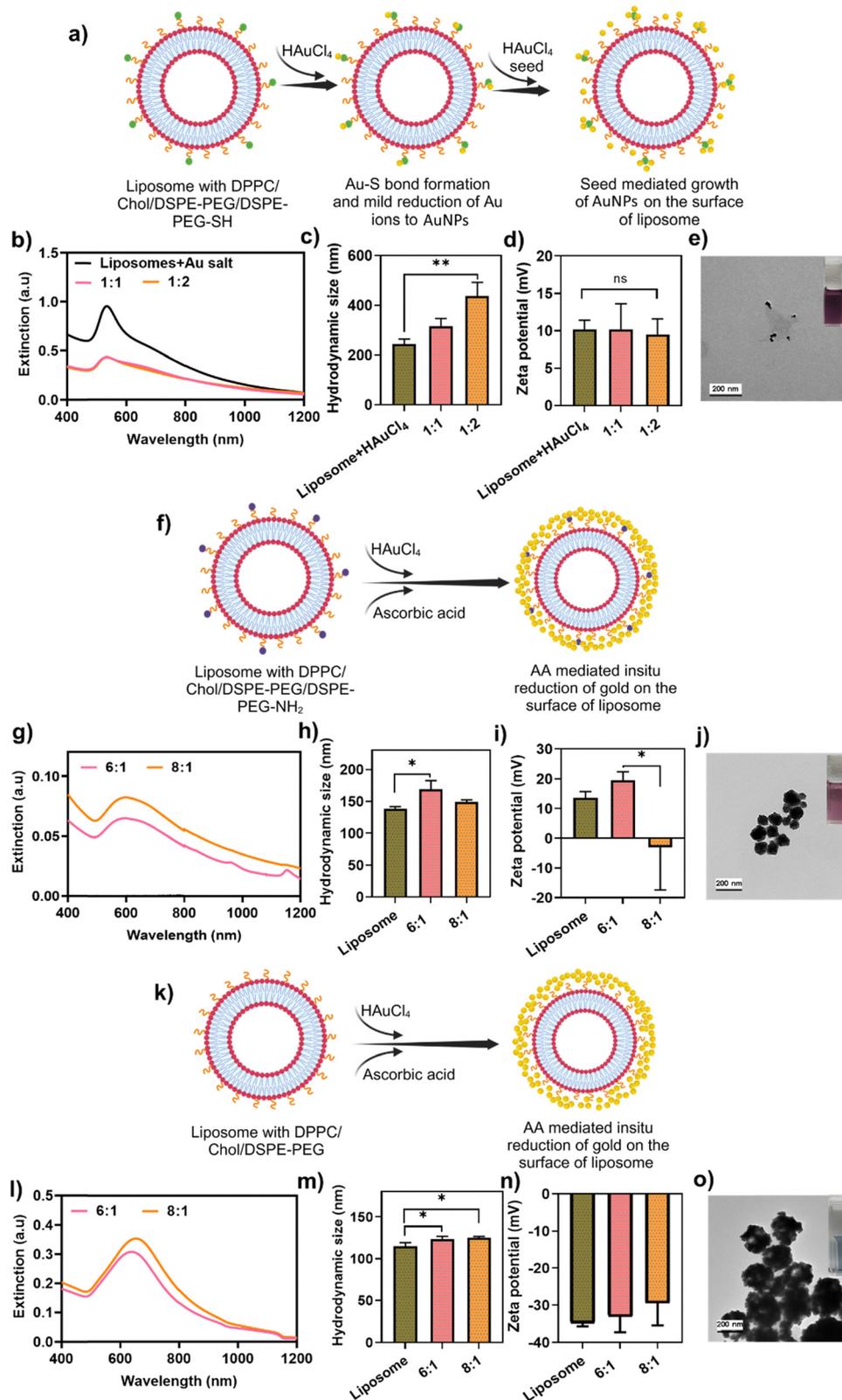
Fig. 1 Synthesis approaches that failed to control opto-mechanical properties of gold–liposome nanohybrids. (a) Schematic representation of gold–liposome nanoparticle synthesis with DPPC/chol/DSPE–PEG/DSPE–PEG–SH liposomes. (b) Extinction spectra of the nanoparticles showing LSPR in the visible region. (c) Hydrodynamic diameter measured using dynamic light scattering, (d) zeta potential showing the surface charge of the different samples. (e) Representative TEM micrograph of the sample with a liposome : gold seed ratio of 1 : 2 (inset: the optical image of the sample in a cuvette). (f) Schematic representation of gold–liposome nanoparticle synthesis using DPPC/chol/DSPE–PEG/DSPE–PEG–NH$_2$ liposomes. (g) Extinction spectra of the nanoparticles showing LSPR in the visible region. (h) Hydrodynamic diameter and (i) surface charge of the two samples with different ascorbic

acid : HAuCl$_4$ ratios. (j) Representative TEM micrograph of the sample with an ascorbic acid : HAuCl$_4$ ratio of 8 : 1 (inset: the optical image of the sample in a cuvette). (k) Schematic representation of gold–liposome nanoparticle synthesis using DPPC/chol/DSPE–PEG liposomes by direct reduction of Au with ascorbic acid (AA). (l) Extinction spectra of the nanoparticles showing LSPR of two different ascorbic acid : HAuCl$_4$ ratios. (m) Hydrodynamic diameter and (n) surface charge of the samples (n = 3 samples per group). (o) Representative TEM micrograph of the sample with an ascorbic acid : HAuCl$_4$ ratio of 8 : 1 (inset: the optical image of samples in a cuvette). Scale bar = 200 nm. Here, * represents a p value < 0.05, ** represents a p value < 0.01 and, *** represents a p value < 0.001 and ns stands for not significant.

amine groups, allows negatively charged Au^{3+} ions to bind to the liposomes. This explains the overall negative surface charge observed for the 8 : 1 ratio (Fig. 1i). TEM micrographs confirmed uniform gold shell growth on the liposomes that aligned well with the change observed in size and surface charge (Fig. 1j). But the TEM image showed that fairly thick gold shells were formed, which not only limited the shift of the LSPR to the NIR necessary for therapeutic benefits, but also limited the control of the stiffness of the final nanoparticles. Indeed, the photothermal profile of these nanoparticles only showed a 4.5 ± 0.3 °C temperature increase insufficient for photothermal therapies (Fig. S1a). In our third approach liposomes composed of PEG terminated lipids without additional amine or thiol moieties were used with the rationale that covalent attachment of Au seeds on these moieties drives discrete nucleation sites that restrict our ability to control the location of gold on the liposomes. Since ascorbic acid mediated reduction of gold was successful in the previous method, a similar approach was followed here with the same ascorbic acid to HAuCl$_4$ ratios, 6 : 1 and 8 : 1 (Fig. 1k). This approach enabled the shift in the LSPR to ~650–700 nm (Fig. 1l) and a desirable size range of 123.7 ± 7 nm and 125.1 ± 1.47 nm for 6 : 1 and 8 : 1 ratios, suggesting an ~10 nm Au shell on the liposomes (115 ± 4.3 nm) (Fig. 1m). The uncoated liposomes have a negative surface charge which minimally changes after gold coating (Fig. 1n). A negative zeta potential for AuNPs synthesized using ascorbic acid methods has been reported previously,[31] attributable to residual chlorine ions from HAuCl$_4$. TEM images confirmed a well distributed AuNP coating on liposomes (Fig. 1o) and photothermal studies showed a rapid increase in temperature suitable for therapies (Fig. S1b). However, this approach did not allow us to control the location of gold on liposomes to modulate the overall stiffness, and the free PEG chains on the liposomes prohibited us to tune the LSPR to the NIR resulting in batch-to-batch variations with unreliable photothermal properties.

Finally, we used liposomes composed of only DPPC lipids and cholesterol to design GLNs with the rationale that any additional lipids or surface moieties would hinder our ability to control the location of gold (Fig. 2a). The use of AA to reduce HAuCl$_4$ (an AA : HAuCl$_4$ ratio of 8 : 1) resulted in the formation of small AuNPs that were deposited inside liposomes and confirmed via transmission electron micrographs (TEM). Without any surface blocking linkers such as PEG, ions (Au^{3+}) and small molecules (AA) could pass through the lipid bilayers into the hydrophilic cavity of liposomes for subsequent reduction. Since we successfully designed GLNs with gold inside the liposomes, we conceded that a well-controlled surface coating is necessary to control gold layers outside liposomes that will

ultimately drive systematic changes in the stiffness. Chitosan was used as a surface coating as it is a biocompatible positively-charged polymer that readily binds to negatively charged liposomes.[32] Here negatively charged Au ions bind to positively charged chitosan via electrostatic attachment and covalent attachment via chitosan's amine groups. After optimization, the chitosan : liposome volume ratio was finalized at 2 : 1 to enable high yield of GLNs without compromising other physicochemical properties. The concentration of chitosan is also critical here as at very high concentration (0.1%, 0.3%) thicker Au shells were formed with visible LSPR and poorly-controlled photothermal properties (Fig. S2). At a lower chitosan concentration of 0.001%, an uneven layer is formed on liposomes leaving gaps on the surface through which Au ions and AA could percolate within liposomes. This resulted in some AuNPs inside liposomes and some outside forming a partial AuNP shell on the surface (Fig. 2b, d and e). At a slightly higher chitosan concentration of 0.01%, a continuous layer was formed on the liposomes resulting in a uniform AuNP shell (Fig. 2c, d, e and Fig. S3). Through this optimized approach three different GLNs were designed for subsequent modulation of cellular behavior. These samples are designated as 0% (no chitosan), 0.001% (low-chitosan) and 0.01% (high-chitosan) GLNs throughout the manuscript. Here TEM micrographs show the overall morphology of the GLNs distinguishing the location of gold on the liposomes is distinct for the three different GLNs (Fig. 2a–d and Fig. S3). Cryo-SEM images show 3D structures in a frozen-hydrated, native-like state providing structural information of the GLNs where 0% GLNs have a smoother topology and 0.01% GLNs have rougher topology (Fig. 2e). Note that sizes in TEM are slightly smaller than that in cryo-SEM and the hydrodynamic size measured using dynamic light scattering (DLS, Fig. 2g). This is because GLNs are not hydrated, i.e. liposomes are dry and collapsed in TEM. Elemental analysis of the GLNs was performed using energy-dispersive X-ray spectroscopy (EDS) coupled to TEM (Fig. S4–S6). Our analysis shows significant differences in the amount of Au in each sample. We also see differences in the carbon content in each sample likely arising from the presence of lipids and chitosan. The extinction spectra show a well-defined LSPR at ~800 nm for 0% GLNs (Fig. 2f), suggesting that AuNPs deposited within liposomes likely form a nanocage-like architecture within the lipid-bilayer enabling LSPR tunability to the NIR.[33,34] The LSPR of the 0.001% GLNs red-shifted to 900 nm showing significant LSPR damping, which may result from both homogeneous and inhomogeneous broadening. Homogeneous broadening of LSPR results from optical excitation of single electron interband transitions that reflect the excitation induced damping of the collective electron oscillation and has been observed in thin shell metal nanoshells. Inhomogeneous
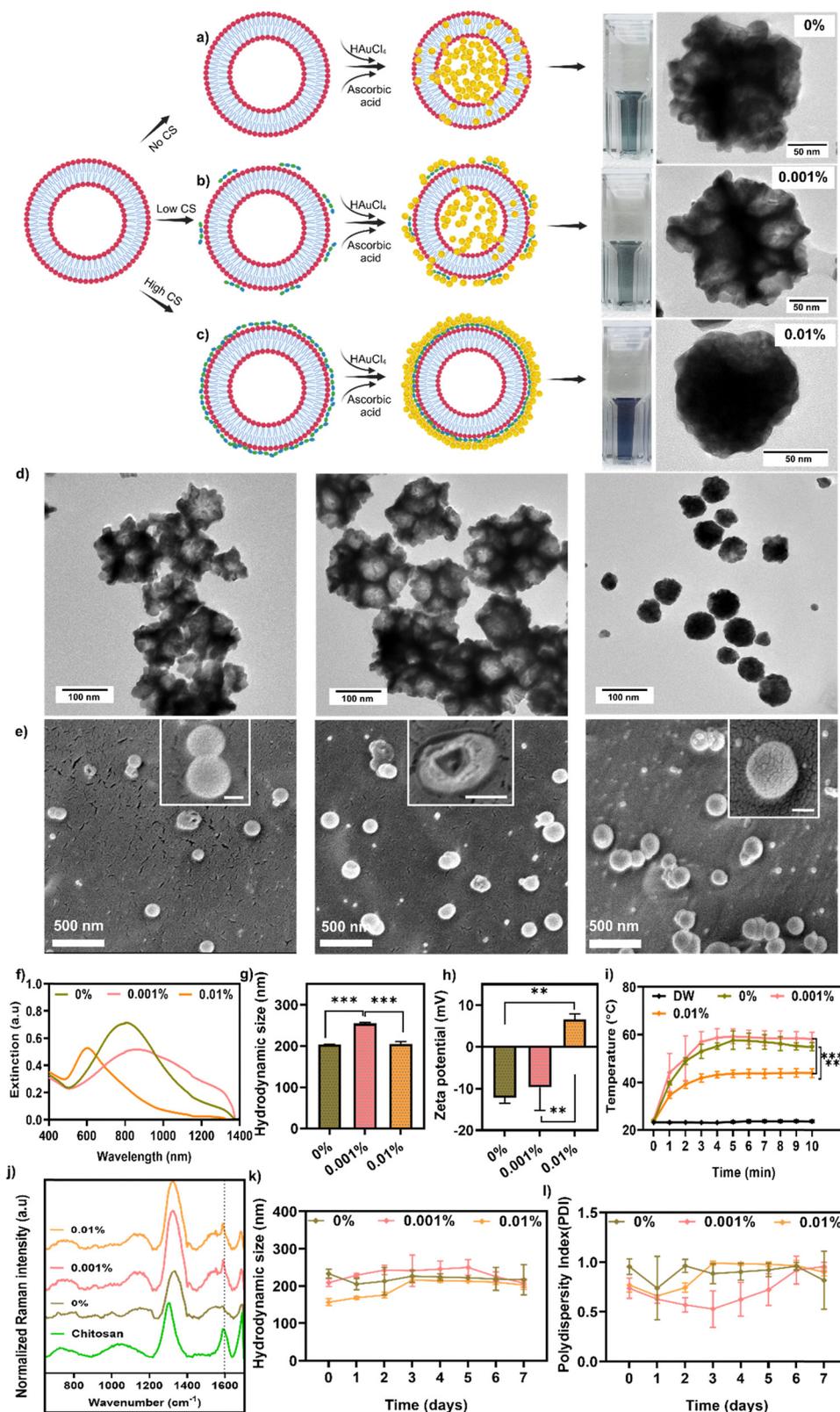
Fig. 2 Synthesis and physicochemical properties of gold–liposome nanohybrids (GLNs). Schematic representation and physicochemical characterization of GLNs synthesized using DPPC/cholesterol liposome and optimized with different concentrations of chitosan layer on liposomes. Illustration created using the Biorender scientific illustration platform. Optical images and high magnification TEM micrographs of the samples of GLNs containing (a) only DPPC/chol liposome without chitosan (0% chitosan), (b) DPPC/chol liposome with low (0.001%) chitosan and (c) DPPC/chol liposome with high (0.01%) chitosan. Scale bar = 50 nm. (d) Low magnification TEM images (scale bar = 100 nm) in the order of 0% GLNs, 0.001% GLNs, and 0.01% GLNs and (e) cryo-SEM images showing 3D structures in a frozen-hydrated, native-like state, revealing structural information in the same order as above.

Scale bar = 500 nm (inset = 250 nm). Note: sizes in TEM are slightly smaller than that in cryo-SEM and the hydrodynamic size is measured using DLS, since GLNs are not hydrated *i.e.* liposomes are dry and collapsed in TEM. (f) Extinction spectra of the GLNs showing tunable LSPR in the near-infrared. (g) Hydrodynamic size, (h) surface charge, and (i) photothermal efficiency of the three GLNs ($n = 3$ samples per group). (j) Normalized Raman intensity spectra of all GLNs ($n = 3$ samples per group). Stability studies of GLNs showing (k) the hydrodynamic size and (l) polydispersity index (PDI) of GLNs up to seven days in MQ water ($n = 3$ samples per group). Here, * represents a p value < 0.05, ** represents a p value < 0.01 and, *** represents a p value < 0.001 and ns stands for not significant.

broadening results from synthesis imperfections of colloidal metal NPs that are often ingrained in the synthesis approach, and in the case of 0.001% GLNs partial deposition of AuNPs inside and partially outside of liposomes contributes to this broadening. The LSPR of the 0.01% GLNs (Fig. 2f) and GLNs synthesized with 0.1% and 0.3% chitosan (Fig. S2a) blue-shifted to the visible region, indicating the formation of thicker Au shells with those concentrations. The size and surface charge varied from bare liposomes to GLNs (Fig. 2g, h and Fig. S7). The surface charge of 0% GLNs (-12.2 ± 1.3 mV) is similar to that of bare liposomes, which confirms that the AuNPs are deposited inside the liposomes. For the 0.01% GLNs, the charge is positive (6.6 ± 1.3 mV), driven by the thicker chitosan layer, and the charge of 0.001% GLNs is in the interim (-9.7 ± 5.5 mV). When excited with an 808 nm diode laser, the photothermal profiles of 0% and 0.001% GLNs with NIR resonance are similar, achieving hyperthermia with therapeutic potential. In contrast, 0.01% GLNs showed a sub-par photothermal profile (Fig. 2i), consistent with their blue-shifted LSPR in the visible region. This reduced heating arises from diminished spectral overlap with the excitation wavelength of the 808 nm laser and increased plasmon damping associated with thicker gold shells, resulting in lower photothermal conversion efficiency. Given the success in designing GLNs with desirable properties using chitosan coating, we also attempted chitosan coating and subsequent AuNP deposition on the DPPC/chol/DSPE–PEG liposomes to see if the LSPR could be shifted to the NIR region (Fig. S8 and S9). But the LSPR peak remained in the visible region for the resulting NPs with minimal extinction in the NIR and no ability to tune the location of gold on the liposomes to control cellular interactions and hence not used in the rest of the study. Raman spectroscopy characterized the presence of chitosan layers (Fig. 2j) with a distinct peak at 1600 cm^{-1} that is visible for the 0.001% and 0.1% GLNs. The peak at 1300 cm^{-1} is attributable to liposomes as shown in the SI (Fig. S10).[35] Thermogravimetric analysis (TGA) assessed the varying degree of gold mass in GLNs (Fig. S11), where bare liposomes rapidly decomposed and GLNs samples showed distinct mass loss depending on the ratio of organic to inorganic content.[36] The GLNs showed long term stability in MQ water for ~2 weeks, suggesting long shelf life (Fig. 2k, l and Fig. S12), and were stable in PBS as well as in cell media for over 24 h (Fig. S12).

The location of gold controls the mechanical properties as GLNs represent a hybrid between soft (liposomes) and hard (AuNPs) NPs. These mechanical properties influence cellular uptake and the pathways NPs take to internalize in cells.[37,38] The stiffness of GLNs was measured (Fig. 3a–c) using bio-atomic force microscopy (Bio-AFM)[39,40] and compared to that of bare liposomes and commercially purchased solid AuNPs of 20 nm and 100 nm as a control to determine the stiffness regime. AFM peak force error (PFE) images (Fig. 3d) provide enhanced contrast to visualize fine surface features; PFE represents an approximate measure of regulation error of AFM feedback-loop. The size analysis using AFM (Fig. 3e) aligns well with the hydrodynamic sizes measured using DLS and TEM (Fig. 2). Stiffness measurements (Fig. 3f) show that soft liposomes have a Young's modulus of 4.01 ± 0.98 MPa, which is equivalent to published reports.[41,42] 0% GLNs had slightly higher stiffness at 11.5 ± 2.27 MPa, which was expected as AuNPs were inside the liposomes and the AFM tip probed the lipid surface of GLNs. The stiffness of 0.001% GLNs with AuNPs both inside and outside liposomes was 19.3 ± 2.28 MPa and that of 0.01% GLNs with AuNPs forming a shell on liposomes was 50.5 ± 4.99 MPa, similar to the stiffness of solid AuNPs (46.3 ± 6.75 for 20 nm and 39.2 ± 7.17 MPa for 100 nm AuNPs). The commercial AuNPs are stabilized using PEG; the 100 nm AuNPs with longer-chain PEG for stability might dampen apparent stiffness in AFM measurements. The stiffness measured for GLNs also accounts for chitosan layers on liposomes as part of the AuNPs shell is likely embedded in chitosan. Whereas solid AuNPs without any coating have GPa range stiffness, AuNPs when coated in soft materials have stiffness in the MPa range, commensurate with our findings (Table S1). Note that mechanosensing of cells is usually sensitive in the 1–1000 kPa range for the substrates they grow on, and < 200 MPa for NPs they uptake (Table S2); cells may reach a saturation point beyond this stiffness. Since our primary goal is to examine cellular interactions of GLNs, which require biopolymers such as chitosan and lipids for enhanced stability and biocompatibility, our stiffness is within the regime that cells can sense and uptake NPs. Thus, in AFM we intentionally maintained the force applied within appropriate limits to avoid rupturing or deformation of the delicate liposomal membrane and preserve the hydrated architecture of the PEG layer, which is the surface cells realistically encounter. Our measurements were carried out in liquid using a ScanAsyst-Fluid probe and analyzed with the Hertz and cone–sphere models (Fig. S13, S14 and Table S3). Whereas piercing the gold core center may serve as a reference point, our measurements were precisely scaled to delineate the biologically relevant, soft nanohybrid interface. Roughness values (R_a) were also measured using AFM, which is an indicator of the surface morphology of GLNs and directly correlates to their surface energy, interfacial interactions, and overall topology. This quantitative measure provides the nanoscale height fluctuations resulting from the topology. Our analysis shows significant differences in R_a values among
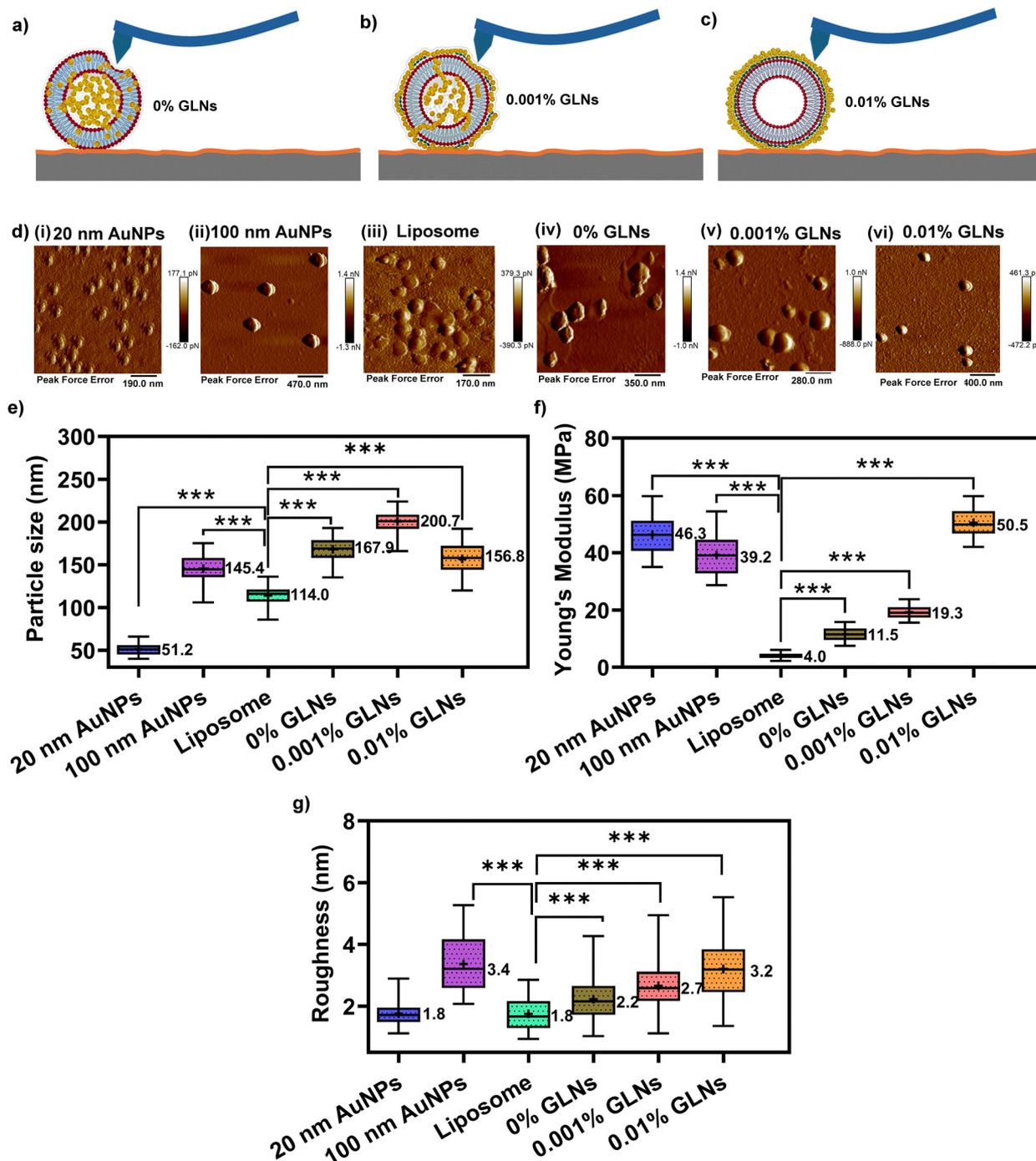
Fig. 3 Mechanical properties and corresponding Young's modulus of gold–liposome nanohybrids (GLNs). (a)–(c) Schematic representation showing how the location of gold on the liposomes influences the stiffness of the resulting GLNs. (d) AFM analysis showing the peak force error images of control nanoparticles that include (i) 20 nm AuNPs, (ii) 100 nm AuNPs, and (iii) bare liposomes, and (iv) GLNs with 0% chitosan, (v) GLNs with 0.001% chitosan, and (vi) GLNs with 0.01% chitosan. The 20 nm AuNPs, 100 nm AuNPs, and bare liposomes are control nanoparticles that allow determination of a range of stiffness for the GLNs. (e) Particle size as measured using AFM ($n = 120$), (f) Young's modulus measured using a cone sphere model ($n = 186$ NPs per sample) and (g) roughness values measured and calculated directly from unfiltered height data ($n \sim 150$–180 per sample). The samples include 20 nm AuNPs (46.3 MPa), 100 nm AuNPs (39.2 MPa), bare liposomes (4 MPa), GLNs with 0% chitosan (11.5 MPa), GLNs with 0.001% chitosan (19.3 MPa), and GLNs with 0.01% chitosan (50.5 MPa). Here, * represents a p value < 0.05, ** represents a p value < 0.01 and, *** represents a p value < 0.001 and ns stands for not significant and (+) represents the mean of each group.

the GLNs, providing indirect evidence of differences in surface topology among the three GLN samples (Fig. 3g).

The cellular uptake of GLNs was assessed in DC2.4 dendritic cells and MODE-K epithelial cells (Fig. 4a) to examine how
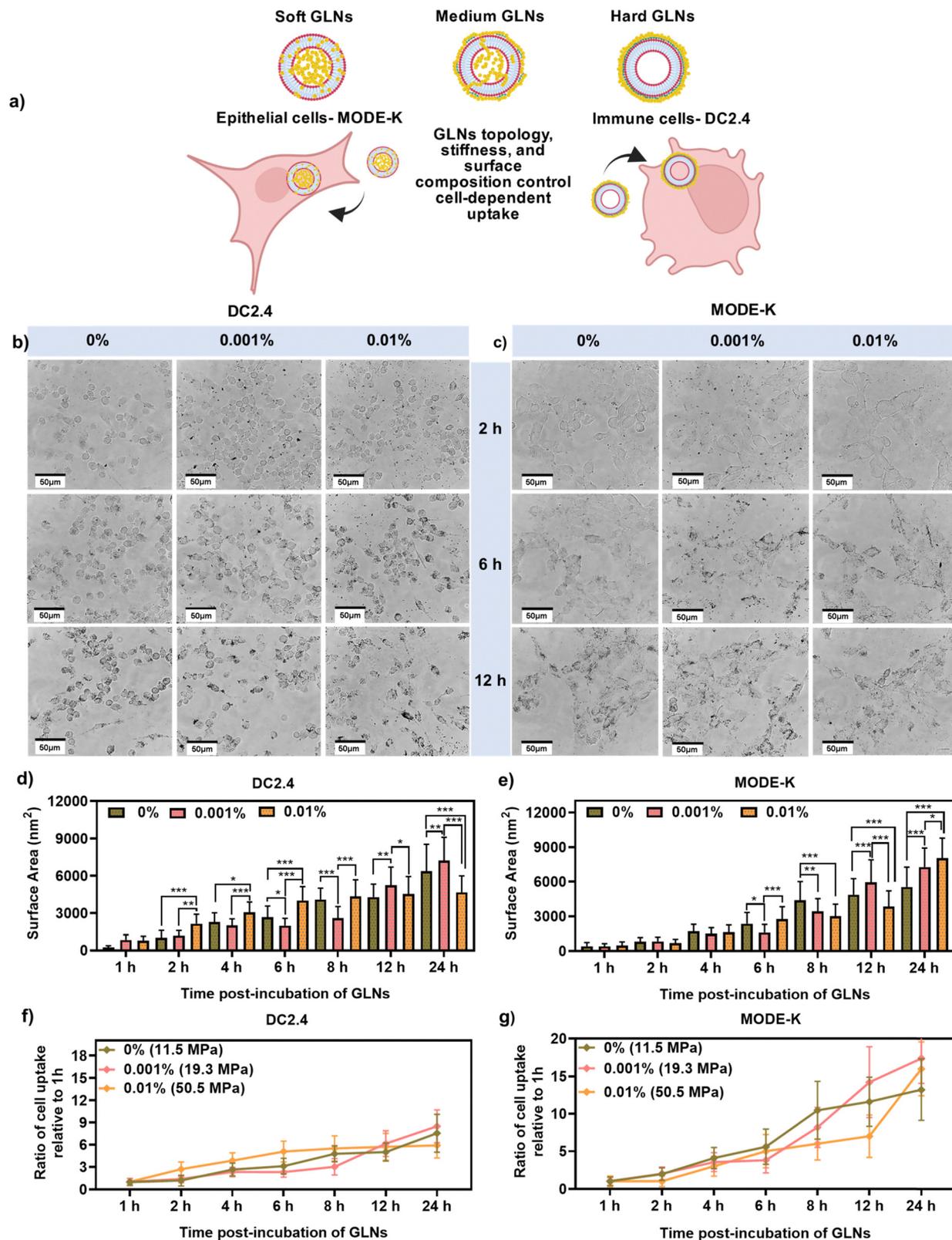
Fig. 4 Cellular uptake determined by gold–liposome nanohybrid (GLN) topology, stiffness, and the cell-type. (a) Schematic showing cellular uptake of GLNs in different cell-types. (b) and (c) Cell uptake *in vitro* of GLNs without chitosan (0%), with 0.001% chitosan and with 0.01% chitosan. Representative white light images at 2 h, 6 h, and 12 h in DC2.4 cells (b) and MODE-K cells (c). Scale bar = 50 μm. Quantification of GLN uptake using ImageJ software in DC2.4 cells (d) and (e) MODE-K cells at different time points measured in $n = 30$ cells for each cell-type and each GLN sample. The ratio of cell uptake at various timepoints relative to uptake at 1 h in (f) DC2.4 cells and (g) MODE-K cells represented for the three different 0%, 0.001%, and 0.01% GLNs with different Young's moduli (stiffness). Here, * represents a p value <0.05, ** represents a p value <0.01 and, *** represents a p value <0.001 and ns stands for not significant.

Table 1 Physicochemical properties of bare liposomes and GLNs including size, charge, stiffness, LSPR, photothermal (PTT) temperature when excited with 808 nm near-infrared laser, and Au concentration equivalent to optical density 0.1 measured using ICP-MS

Sample name	Hydrodynamic size (nm)	Zeta potential (mV)	Young's modulus (MPa)	LSPR (nm)	PTT temp. @ 5 min (°C)	Au Conc. (μg mL^{-1})
Liposome	138.4 ± 1.4	−12.9 ± 6.6	4.01 ± 0.98	—	—	—
0% GLNs	202.9 ± 1.3	−12.2 ± 1.3	11.5 ± 2.27	805	57.5 ± 3.8	0.28
0.001% GLNs	254.3 ± 3.4	−9.7 ± 5.5	19.3 ± 2.28	860	59.2 ± 3.1	0.48
0.01% GLNs	204.7 ± 6.2	6.6 ± 1.3	50.5 ± 4.99	602	43.6 ± 1.5	0.62

topology (smooth/uneven/textured), surface molecular composition (lipid-rich/inorganic gold), and stiffness (4–50.5 MPa) direct cell-interactions. Cell viability of GLNs showed minimal toxicity across concentrations (Fig. S15). The concentration of GLNs ideal for visualizing the uptake studies was determined by first incubating the 0.001% GLNs as a representative in both cell-types for 6 h at different doses corresponding to Au concentrations between 2.5 and 15 μg mL^{-1} (Fig. S16). The 5 μg mL^{-1} concentration appeared to be neither too sparse nor too aggregated for the brightfield imaging and was selected for further uptake studies. The Au content of the GLNs was determined using inductively coupled plasma mass spectrometry (ICP-MS) analysis (Table 1). The uptake corresponding to 5 μg mL^{-1} Au was found to have quantifiable differences at different timepoints; this concentration was then used for all three GLNs for cellular uptake (Fig. 4b–g and Fig. S17). GLNs have a clear contrast in brightfield images appearing as black dots enabling quantification of those internalized in cells via ImageJ. The total surface area of GLNs was measured in 30 cells for each cell-type and for each GLN sample (Fig. 4d and e). The black dots do not represent single particles but clusters of GLNs, and therefore surface area is an accurate measure of uptake. Our findings show that uptake was temporally-controlled and varied significantly for the three GLNs and also by cell-type. Uptake was faster in DC2.4 within 2 h post-incubation (Fig. 4d) and slower in MODE-K cells (Fig. 4e) where differences among the GLNs were observed at 6 h post-incubation. Our analysis focused on within-cell-type kinetics (1–24 h) to capture uptake trends and avoid direct quantitative comparison between DC2.4 and MODE-K as cell size and polarity introduce confounders that can bias per-cell measurements. Furthermore, 0% GLNs demonstrated a slow but consistent increase in internalization in both cells, likely because cells are interacting with a smooth topology, negative surface-charge, and a lipid/cholesterol-rich surface. The hydrophilic phosphate groups of lipids likely enable fusion of 0% GLNs with cell membranes facilitating slow but steady endocytosis. Comparatively, 0.001% GLNs with a similar size to 0% GLNs and negative surface charge showed a lower uptake in both cell-types in the initial 8 h post-incubation. Images showed that residual 0.001% GLNs remained outside the cells at these timepoints. At 12 h and 24 h post-incubation, uptake increased for 0.001% GLNs and exceeded that of 0% GLNs. The slow initial rate of endocytosis of 0.001% GLNs is attributed to the highly uneven topology and mixed molecular composition including lipids and AuNPs. The uneven surface topography

also increases the overall surface area available to cells,[20] enhancing cellular-interactions and promoting internalization at later timepoints. The 0.01% GLNs with a similar size but a positive charge demonstrated highly cell-dependent uptake across timepoints; here cells encounter a textured topology and interact with inorganic AuNPs on the surface. We find that 0.01% GLNs have the highest and fastest uptake in DC2.4 but reach their capacity at 8 h, indicating a saturation-point in uptake. In MODE-K cells, 0.01% GLNs showed a slow initial uptake and overall higher uptake than DC2.4 at 24 h. This was surprising as antigen-presenting cells are known to readily uptake AuNPs, but this observation could be attributable to the abundance of chitosan. Chitosan increases interactions with epithelial cells by modulating cell-permeability through paracellular and intracellular pathways.[43]

Next, we examined how GLN stiffness impacts internalization by quantifying the ratio of uptake at various timepoints relative to uptake at 1 h, which serves as a baseline as minimal GLNs are internalized at 1 h (Fig. 4f and g). We find that at early timepoint (2 h, 4 h) MODE-K cells showed no differences in uptake as a function of stiffness, but in DC2.4, significant differences among the three GLNs were seen. Hard 0.01% GLNs had a higher uptake in DCs at early timepoints but soft 0% GLNs and intermediate stiffness 0.001% GLNs had higher uptake at later timepoints. These trends are reversed in MODE-K where 0.01% GLNs have higher uptake at later time-scales (24 h), whereas 0% GLNs show higher internalization at intermediate timescales (~8 h). Furthermore, the slope of the longitudinal uptake significantly varies by GLN stiffness for each cell-type. The 0.01% GLNs demonstrate a steep slope in early uptake kinetics in DCs but reach a saturation point within ~8 h. In MODE-K, 0.01% GLNs show a shallow slope in uptake kinetics, which rapidly increases after 12 h. Of note is the intermediate stiffness 0.001% GLNs that show a slow but steady uptake in both cell-types. Dendritic cells are less deformable and prefer harder NPs that can engage with the cellular receptors leading to more effective uptake.[44] Epithelial cells (such as cancer cells) internalize softer particles more rapidly.[21,45] However, our findings go beyond the current paradigm and suggest that (1) uptake is temporally-controlled and cell-type dependent for the three GLNs and (2) cells are highly sensitive to the endocytosis rate despite a narrow range of stiffness of GLNs studied here. Note: a higher stiffness range can be achieved by increasing Au shell thickness on the liposomes; however, that would also substantially influence the size. The size of NPs dominates all cellular processes, and the
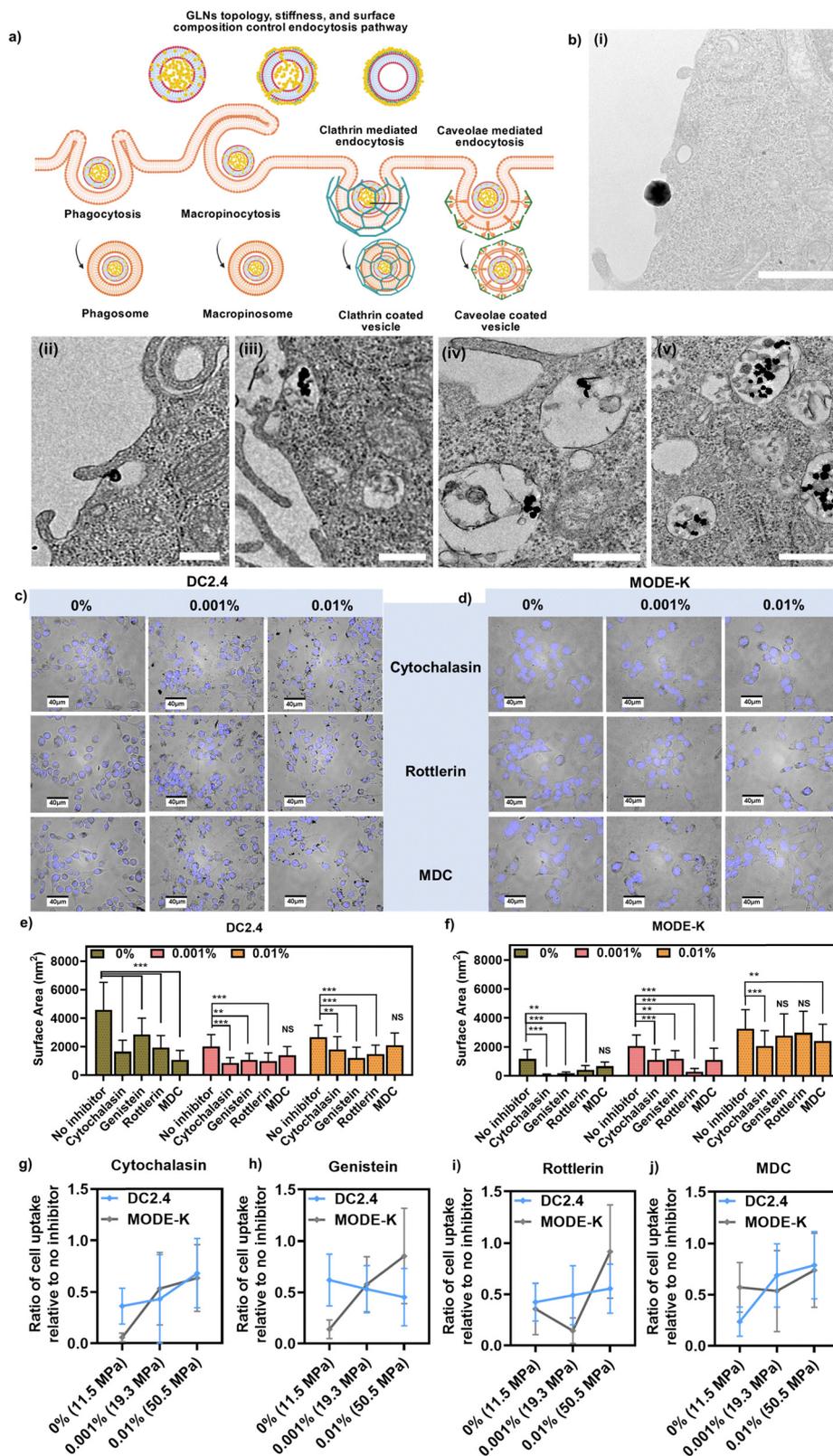
Fig. 5 Endocytosis pathways controlled by gold–liposome nanohybrid (GLN) topology, stiffness, and the cell-type. (a) Schematic of endocytosis pathways GLNs use to enter cells. (b) TEM micrographs of GLNs showing (i) interaction with cells, (ii)–(iv) internalization *via* macropinocytosis, (v) presence in other cellular vacuoles. Scale bar = 500 nm for all images. GLNs without chitosan (0%), with 0.001% chitosan and with 0.01% chitosan incubated for 6 h in cells pre-treated with different inhibitors corresponding to different endocytosis pathways. Representative overlay images of brightfield and DAPI (blue) in (c) DC2.4 and (d) MODE-K cells. Scale bar = 40 μm. Here cytochalasin B inhibits phagocytosis, rottlerin inhibits macropinocytosis, and monodansyl cadaverine (MDC) inhibits clathrin-mediated endocytosis. Quantification of GLNs uptake *via* different endocytosis

pathways in (e) DC2.4 cells and (f) MODE-K cells measured in $n = 30$ cells for each inhibitor and each GLN sample. (g)–(j) The ratio of cell uptake relative to no inhibitor in DC2.4 and MODE-K cells for the various endocytosis pathways represented for the three different GLNs with different Young's moduli (stiffness). Here, * represents a p value < 0.05, ** represents a p value < 0.01 and, *** represents a p value < 0.001 and ns stands for not significant.

subtle contributions of NP topology and stiffness may be completely overlooked. We validated our uptake studies with ICP-MS analysis of gold in cells, which generally showed similar trends (Fig. S18). But with bulk measurements, as in ICP-MS, inaccuracies are expected as during sample preparation, GLNs attached to the culture well surface may also be included in measurements. Our image-based single-cell analysis enables an accurate quantification of cellular uptake kinetics.

Next, we examined the endocytosis pathways GLNs utilize to enter cells where our hypothesis is that the topology, surface composition, and stiffness will determine whether GLNs take a single or multiple pathways to enter cells. We used well-established chemical inhibitors to inhibit various pathways in the cells that include: cytochalasin B (10 µg mL^{-1}, 2 h) to inhibit phagocytosis, genistein (200 µM, 1 h) to inhibit CavE, rottlerin (2 µM, 30 min) to inhibit macropinocytosis, and monodansyl cadaverine (200 µM, 10 min) to inhibit CLME.[46] The cell viability of these inhibitors was examined in both cell lines to ensure the specific concentrations and total time we chose were not toxic (Fig. S19). TEM micrographs of GLNs in cells demonstrated the endocytosis process. We were specifically able to capture GLNs interacting with the cell surface (Fig. 5b-i) and then entering cells through macropinocytosis where membrane ruffles enclose GLNs (Fig. 5b-ii). This is followed by the ruffles folding back on the cell membrane undergoing membrane fission to form macropinosomes and GLNs endocytosed in these vesicles (Fig. 5b-iii and iv). GLNs were also found in other vacuoles that may be phagosomes (Fig. 5b-v). Note that GLNs also use other pathways, and therefore for a more comprehensive understanding of the endocytosis, the cells were incubated with each inhibitor followed by addition of GLNs (5 µg mL^{-1}) for 6 h, a timepoint determined from uptake studies and our previous studies.[46] The total surface area of GLNs was measured in 30 cells for each cell-type. The representative images and quantification (Fig. 5c–f and Fig. S19) showed that GLNs use multiple pathways to enter cells and that vastly differs by the cell-type and among the GLN samples. In DC2.4, the 0% GLNs (smooth topology, lipid-rich surface) involve all four classical pathways during endocytosis. This trend aligns with prior studies that show lipid-based NPs are predominantly internalized through many endocytosis mechanisms.[47] However, 0.001% GLNs and 0.01% GLNs do not involve the CLME pathway. This finding was surprising given that solid AuNPs and chitosan-coated NPs are known to involve CLME,[48,49] suggesting that hybrid NPs such as GLNs with uneven or textured surface topology and a mixed surface may avoid clathrin-coated pits and the constituent proteins during internalization in DCs. This also aligns with previous studies that suggest DCs prefer clathrin-independent pathways during NP internalization.[50] In MODE-K, GLNs utilize different endocytosis pathways relative to DCs. For the 0.001%

and 0.01% GLNs, the CLME pathway is involved during uptake but not for 0% GLNs, suggesting that CLME is highly variable by cell-type. Furthermore, we find that phagocytosis is involved in the uptake of all three GLNs in MODE-K cells even though epithelial cells are not as active as professional phagocytes such as DCs. Epithelial cells are often described as facultative or non-professional phagocytes as they also protect against invading pathogens by modulating the actin cytoskeleton and form membrane ruffles that engulf pathogens. This phagocytic property of epithelial cells has been leveraged by micro/nanoparticles in cells.[51] Furthermore, epithelial cells often prefer CavE to internalize NPs in the 200–500 nm size regime.[52] However, this well-accepted principle does not uniformly apply to hybrid NPs; we find that 0.01% GLNs do not use either CavE or macropinocytosis for internalization.

We next examined how the stiffness of GLNs impacts endocytosis. We presented the ratio of cellular uptake of GLNs (Fig. 5g–j) in the presence of a specific inhibitor relative to no inhibitor. A lower ratio indicates that GLNs are highly sensitive to the specific inhibitor and have strongly used that pathway for endocytosis, while a higher ratio indicates the specific inhibitor has a minimal impact and GLNs are less-dependent/independent of that pathway. In DC2.4 we find a clear stiffness-mediated internalization of GLNs via phagocytosis and CLME but minimal impact from CavE and macropinocytosis. The ratio increased with an increase in stiffness, suggesting that hard 0.01% GLNs were less-dependent on these pathways compared to the soft 0% GLNs. Furthermore, soft 0% GLNs utilize both non-receptor-mediated (phagocytosis) and receptor-mediated (CLME) endocytosis in DC2.4.[26] Comparatively, in MODE-K stiffness-dependent internalization of GLNs was observed via phagocytosis, CavE and macropinocytosis but minimal impact from CLME. Furthermore, we find that soft 0% GLNs preferred both non-receptor-mediated (phagocytosis) and receptor-mediated (CavE) endocytosis in MODE-K, whereas intermediate stiffness 0.001% GLNs prefer only non-receptor-mediated endocytosis (macropinocytosis) for internalization. These findings suggest that surface topology, stiffness, and molecular composition of the NP surface collectively drive uptake in cells, and the cell-type determines the pathways NPs leverage for endocytosis.

Next, we examined how the physicochemical properties of GLNs drive their therapeutic ability when excited with an NIR 808 nm laser initiating photothermal ablation in MODE-K cells and photothermal stimulation of immune function in DC2.4. Such therapeutic behavior is governed by the dosage of NPs and the timepoint of analysis. Whereas 5 µg mL^{-1} was ideal for visualizing cellular uptake, our initial studies indicated that a higher GLN concentration along with 6 h–8 h incubation time was required to achieve sufficient GLN uptake and notable therapeutic efficacy in the cells. Thus, we varied the concentration
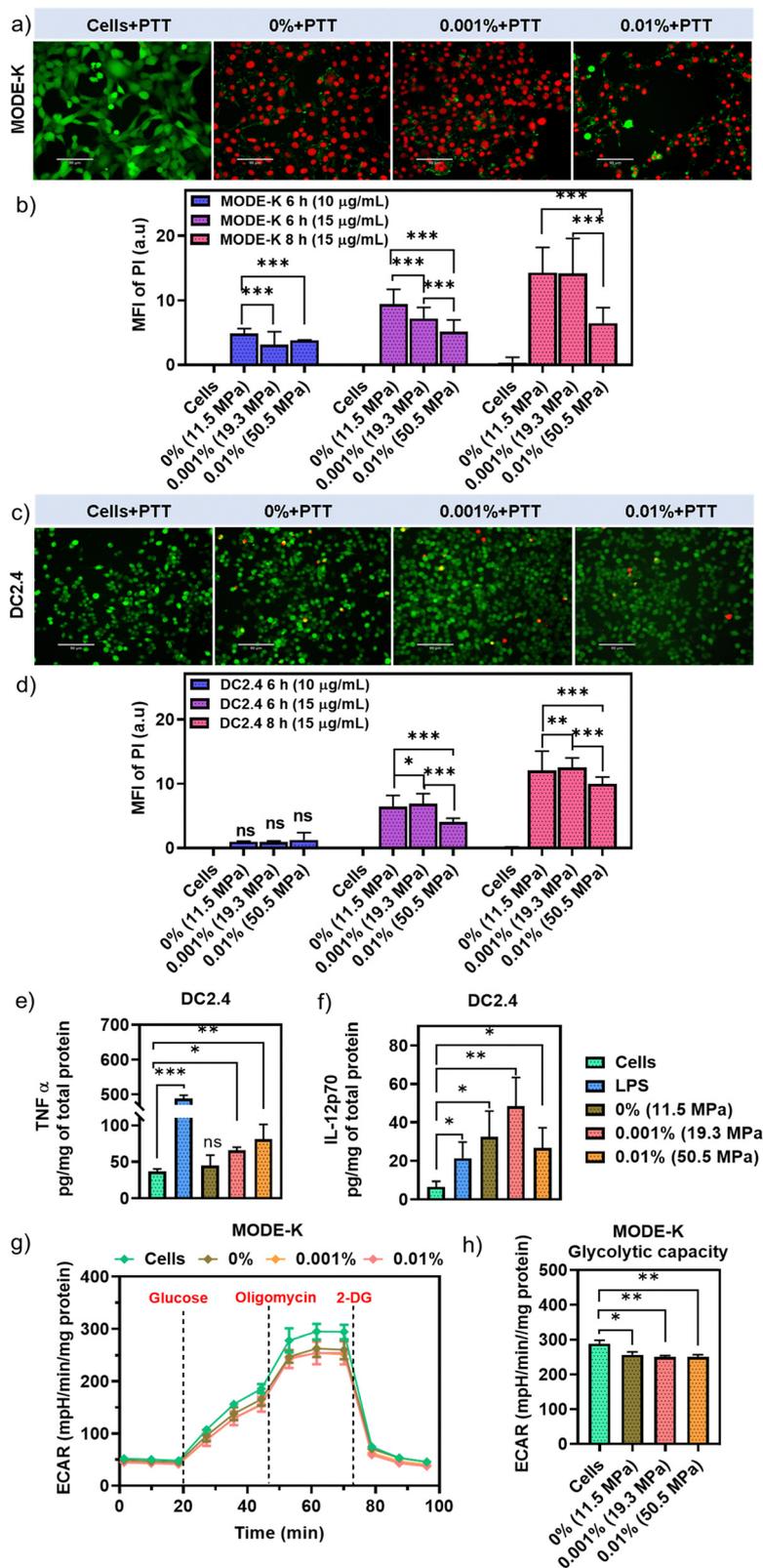
Fig. 6 Photothermal therapeutic ability of GLNs (0%, 0.001%, and 0.01%) and corresponding cytokine and metabolic changes. (a) Representative images of MODE-K cells stained with calcein/propidium iodide (PI) live/dead assay after incubation of 15 μg mL^{-1} of the different GLNs for 8 h. (b) Quantification of the mean fluorescence intensity of PI in MODE-K cells at different concentrations (10 and 15 μg mL^{-1}) and timepoints (6 h and 8 h) obtained using ImageJ ($n \sim$ 150 cells per group). (c) Representative images of DC2.4 cells stained with calcein/PI after incubation of 10 μg mL^{-1} GLNs for 6 h. ($n \sim$ 50 cells per group, scale bar = 90 μm). (d) Quantification of the mean fluorescence intensity of PI in DC2.4 cells at different concentrations (10 and 15 μg mL^{-1}) and timepoints (6 h and 8 h). Cytokine analysis showing (e) TNF-α and (f) IL12-p70 from the DC2.4 cell supernatant collected after treatment

with 10 μg mL^{-1} GLNs for 6 h and photothermal treatment. (g) Measurement of the extracellular acidification rate (ECAR) in response to modulators (glucose, oligomycin, and 2-DG) and (h) quantification of glycolytic activity in MODE-K cells treated with GLNs and photothermal treatment. Here, * represents a *p* value <0.05, ** represents a *p* value <0.01 and, *** represents a *p* value <0.001 and ns stands for not significant.

of GLNs (10 μg mL^{-1}, 15 μg mL^{-1}) and the incubation time (6 h, 8 h) in DC2.4 and MODE-K cells to determine the ideal dosage and timepoint of analysis. Here, MODE-K is broadly representative of diseased epithelial cells (such as cancer cells and neural cells) to expand our approach to various disorders. Calcein/propidium iodide (PI) live/dead cell imaging in both cells (Fig. 6a, c and Fig. S20) incubated with GLNs and quantification of the PI signal (with ImageJ, Fig. 6b and d) determined the therapeutic behavior. In both cell-types, increasing GLN concentration and incubation time increased the PI signal as would be expected for higher photothermal conversion and higher cell death. However, therapeutic trends differ in each cell-type for the different GLNs. In MODE-K, 0% GLNs with smooth topology, lipid-rich surface, and softest stiffness had a higher therapeutic ability than the other GLNs, while 0.01% GLNs with textured topology, inorganic AuNP surface, and hardest stiffness had reached a therapeutic saturation with minimal change across doses and incubation time. These trends align with our earlier results (Fig. 2i) where 0.01% GLNs with visible LSPR showed lower photothermal heating, and the trends also align with uptake studies (Fig. 4e and g) where 0.01% GLNs had lower uptake at the 8 h timepoint relative to the other GLNs. Our findings can be leveraged to design treatment studies in the future for desired outcomes; for example, for high photothermal temperatures 0% and 0.001% GLNs would be more appropriate whereas for mild hyperthermia 0.01% GLNs may be more desirable.

In DC 2.4, at the lower concentration (10 μg mL^{-1}) and shorter incubation time (6 h), all three GLNs have minimal cell death as indicated by PI signal quantification. At higher concentration (15 μg mL^{-1}) and longer incubation time (8 h), the 0.01% GLNs consistently have lower cell death than the other GLNs. This is contrary to the trends observed in uptake studies (Fig. 4d and f) where 0.01% GLNs had higher uptake at both 6 h and 8 h relative to the other GLNs. This suggests that while topology, stiffness, and surface composition of GLNs are critical for cellular uptake and endocytosis pathways they leverage, optimization of optical properties is more critical for photothermal efficiency. Yet all of these properties collectively determine their therapeutic behavior *in vitro*. Note that our goal with DCs is photothermally-mediated immunostimulation with minimal cell death. Therefore, we chose the samples that were incubated for 6 h with 10 μg mL^{-1} of GLNs for cytokine analysis to examine immune function. Cytokine analysis (Fig. 6e and f) shows a distinct profile for each GLN that also varied for the type of cytokines assessed. The 0.001% GLNs evoked a higher IL-12p70 response in DC2.4, whereas 0.01% GLNs evoked a higher TNF-α response. This suggests that both the photothermal efficiency and mixed surface composition may govern their immunostimulation ability and also due to partially exposed chitosan polymers on its surface leading to enhanced secretion of different cytokines.[53] Furthermore, we also performed a Seahorse real-time extracellular flux analysis focusing on

measuring the extracellular acidification rate (ECAR) as a key indicator of glycolytic activity and metabolic stress. Our findings show that photothermal irradiation limited the ability of MODE-K cells to adapt to metabolic stress, as indicated by a significant reduction in their glycolytic capacity compared to untreated cells (Fig. 6g, h and Fig. S21). Despite differences in uptake among the GLNs, no formulation-specific effects were observed, suggesting that photothermal stress predominates over material composition. Note that in this study, we only assessed glycolysis as a readout of metabolic response. While photothermal irradiation reduced glycolytic activity, other pathways including mitochondrial function, ROS generation, and stress-response signaling may also be affected and contribute to cell death but were not evaluated here. Collectively, the therapeutic trends observed here can be leveraged to achieve desired outcomes in the future of either photothermal actuation or immune activation by altering the parameter space of GLNs. Whereas this study focuses on *in vitro* evaluation of how topology, surface moieties, stiffness and photothermal properties of GLNs collectively drive cellular interactions, our future work will be expanded *in vivo* to understand how these characteristics can be leveraged for superior diagnostic and therapeutic function of GLNs to further assess their translational potential.

Conclusions

In summary, our findings show that the location of gold in GLNs enables unprecedented tunability of their topology, surface molecular composition, stiffness, and photothermal conversion, which extends beyond the well-established paradigm of size, shape, and charge. These physicochemical properties of GLNs collectively direct cell-specific internalization in DC2.4 and MODE-K, the rate of uptake, and the endocytosis pathways they use, which are temporally-controlled in each cell-type. We find that surface composition and stiffness are critical parameters in determining endocytosis rates. Our findings also show that when excited with a NIR laser GLNs enable photothermal ablation in MODE-K cells and photothermal immunostimulation in DC2.4, where the topology and resulting LSPR and the surface molecular composition determine which GLN samples can be leveraged to design future therapeutic applications. We envision that our study will ultimately establish new mechanisms that break existing paradigms allowing the design of a class of new NPs to study cellular interactions beyond the cell types investigated here. Such NP–cellular interactions will enable the development of biomedical imaging techniques and therapies for treatment of cancer,[54,55] cardiovascular diseases,[56] and neurological disorders[57] among others. The fundamental underpinnings established through our work will provide design rules correlating traditional NP properties of size, shape, and

charge to the stiffness, topology, and surface ligands to direct stimuli-controlled diagnostic and therapeutic function.

Materials and methods

Materials

Chitosan was purchased from Sinopharm Chemical Reagent Co., Ltd, China. Gold(III) chloride, trisodium citrate, and sodium borohydrate were obtained from Sigma Aldrich, St. Louis, MO. Ascorbic acid was obtained from Sigma Aldrich, Germany. Cholesterol, 2-[4-(2-hydroxyethyl)piperazin-1-yl]ethanesulfonic acid (HEPES), and sodium chloride (NaCl) were bought from Sigma–Aldrich (Chicago, IL). 1,2-Distearoyl-sn-glycero-3-phosphoethanolamine-N-[methoxy (polyethylene glycol)-2000] (DSPE–PEG), 1,2-dipalmitoyl-sn-glycero-3-phosphocholine (DPPC), and (1,2-distearoyl-sn-glycero-3-phosphoethanolamine-poly(ethylene glycol)-amine) (DSPE–PEG–NH$_2$) were purchased from Avanti Polar Lipids (Alabaster, AL). Chloroform was purchased from Fisher Scientific (cat#C298–500). 20 nm ultra uniform gold nanospheres (SKU: AUXU20-1 M) and 100 nm ultra uniform gold nanospheres (SKU: AUXU100-1 M) were purchased from nanoComposix, San Diego, CA.

Methods

Preparation of liposomes and gold–liposome nanohybrids. All liposomes were prepared through a thin film hydration technique utilizing varying amounts of lipid ratios.[58–60] Briefly, lipids of appropriate ratios for each type of liposome were dissolved in 1 mL of chloroform (99.8% purity) to form a homogenous mixture. After a thorough mixing of these lipids, the chloroform is removed using a nitrogen stream in the fume hood. Furthermore, the lipid film is completely dried overnight using a vacuum oven at room temperature. Once the thin lipid film is made, it is further hydrated using 10 mL of HEPES (20 mM) containing 140 mM NaCl buffer and stirred for 45 minutes. The temperature was maintained above the gel–liquid crystal transition temperature (T_c) of the lipid with the highest T_c, which is 55 °C. This agitation and temperature were maintained for an hour. Following this, the liposomal solution was subjected to 5 freeze–thaw cycles for 5 min each. Then, the desired sizes of liposomes were achieved using extrusion (Lipex 10 mL extruder, Evonik Canada Inc.). This was again done at a temperature of 55 °C. The size of the liposomes was checked for every cycle after the 3rd extrusion cycle to make sure the desired size was obtained. Once the liposomes of size 120–130 nm were obtained, extrusion was stopped, and the liposomes were washed with Milli-Q water using a 100 kDa MWCO filter (Amicon Ultra-4, Merck Millipore (Darmstadt, Germany)) and resuspended to a concentration of approx. 3.5 mg mL^{-1} based on the lipid weight. The thiol liposomes were synthesized using DPPC, cholesterol, DSPE–PEG, and DSPE–PEG–SH taken at the mass ratio of 1800 : 1200 : 1260 : 540 μg. The thiol terminated lipid (DSPE–PEG–SH) was synthesized by thiolation of DSPE–PEG NH$_2$ using Traut's reagent.[61] Briefly, 6.2 mg of Traut's reagent was dissolved in 50 μL of methanol and added to 25 mg

of DSPE–PEG-$_{2K}$-amine dissolved in 1 mL of chloroform. The solution was stirred at room temperature for 2 h and the chloroform was evaporated completely. The residue was dissolved in PBS with 25 mg of (tris(2-carboxyethyl) phosphine) (TCEP) for 1 h and dialyzed using a 1 kDa MWCO cellulose membrane overnight. The dialysate was lyophilized and stored until further use. The quantification of sulfhydryl groups was performed by DTNB assay using N-acetyl cysteine for the preparation of the standard SH calibration curve.

Gold coating of thiol liposomes. The gold coating technique for these liposomes consisted of a pre-coating of 0.25 mM HAuCl$_4$ followed by mixing with gold seeds. The liposomes were incubated with 1 mL of 0.25 mM gold(III) chloride (HAuCl$_4$) for 1 h. The gold seed was prepared using 0.25 mM HAuCl$_4$ and 0.25 mM trisodium citrate (Na$_3$C$_6$H$_5$O$_7$) in 10 mL of Milli-Q water, to which 60 μL of ice cold 0.1 M sodium borohydrate (NaBH$_4$) was added under strong stirring. NaBH$_4$ acts as a reducing agent, reducing the gold chloride to gold nanoparticles. The gold seed was allowed to age at room temperature for 30 minutes in the dark. The experimental setup consisted of liposomes and the gold seed in 3 volume ratios such as 1 : 0, 1 : 1, and 1 : 2. The liposomes, after the addition of gold seeds, were allowed to react for 3 h, after which the gold-coated liposomes were pelleted down by centrifuging at 15 000 rpm for 20 minutes at 4 °C.

Gold coating of amine liposomes. The amine liposomes were synthesized using DPPC, cholesterol, and DSPE PEG NH$_2$ in the mass ratio of 600 : 400 : 600 μg. The gold coating technique used for amine liposomes was in situ reduction of gold using 20 mM ascorbic acid and 2.5 mM HAuCl$_4$ taken in ratios of 6 : 1 and 8 : 1. To 200 μL of liposome solution, 8 μL of 2.5 mM HAuCl$_4$ and 6 or 8 μL of 20 mM ascorbic acid were added and incubated for 30 min in ice. The solution was centrifuged and washed using Milli-Q water at 6000 rpm for 20 min, resuspended in Milli-Q water, and used for further studies.

Gold coating of DPPC/chol/DSPE–PEG liposomes. The PEG liposomes were synthesized using DPPC, cholesterol, and DSPE PEG in the mass ratio of 600 : 400 : 600 μg followed by in situ reduction of gold using 20 mM ascorbic acid and 2.5 mM HAuCl$_4$ in ratios of 6 : 1 and 8 : 1. To 200 μL of liposome solution 8 μL of 2.5 mM HAuCl$_4$ and 6 or 8 μL of 20 mM ascorbic acid were added and incubated for 30 min in ice. The solution was centrifuged and washed using Milli-Q water at 6000 rpm for 20 min, resuspended in Milli-Q water, and used for further studies.

Gold coating of DPPC/chol liposomes. The DPPC–cholesterol liposomes were synthesized using DPPC and cholesterol in the mass ratio of 600 : 400 μg followed by chitosan coating. Different concentrations of chitosan (0.001%, 0.01%, 0.1%, and 0.3%) were prepared in 0.1 M acetic acid (5 mL), and a 2 : 1 chitosan to liposome volume ratio was used for preparing chitosan coated liposomes. Briefly, an appropriate volume of chitosan solution was added dropwise to the liposome solution under strong stirring and further incubated for 1 h at room temperature and purified using a 100 kDa MWCO filter. *In situ*

reduction of HAuCl$_4$ was performed by adding 8 µL of 20 mM ascorbic acid and 8 µL of 2.5 mM HAuCl$_4$ into 200 µL of the final solution of bare liposome or chitosan coated liposome and incubated in ice for 30 min. After the *in situ* reduction, the solution was centrifuged and washed using Milli-Q water at 6000 rpm for 20 min, resuspended in Milli-Q water, and used for further studies.

Physiochemical characterization of liposomes and gold–liposome nanohybrids. The optical properties of gold–liposome nanohybrids resulting from SPR were measured using a UV-vis-NIR spectrophotometer (Agilent technologies, Inc., Texas). The average hydrodynamic diameter and zeta potential of bare liposomes, chitosan coated liposomes, or gold liposome nano-hybrids were measured by a dynamic light scattering technique (DLS) using a Zetasizer Nano Z (Malvern Instruments, Malvern, UK). All samples were analyzed in triplets ($n = 3$). The morphology of the liposomes or GLNs was evaluated using a scanning/transmission electron microscope (STEM) (200 kV JEOL 2100, JEOL Ltd, Japan) and scanning electron microscope (SU3800, Hitachi). Elemental analysis of the GLNs was performed using energy-dispersive X-ray spectroscopy (EDS) coupled to STEM.

Raman spectroscopy. A Renishaw inVia Raman confocal microscope with a 785 nm laser was used to take scans of the dried free liposomes, free chitosan and liposomes with 0%, 0.001% and 0.01% chitosan using WiRE 5.4 software. The spectrophotometer was calibrated using silica wafer at 520.7 nm. 3 µL of the sample was dried on a 2 mm CaF$_2$ disk for 20 minutes at 37 °C. The samples were run under a 50× objective with 100% laser.

Thermogravimetric analysis. The thermogravimetric analysis was done using a Netzsch STA449F1 TGA system. Samples of free liposomes, 0%, 0.001% and 0.01%, approximately 3 mg, were transferred to aluminium crucibles. The experiment was done under nitrogen gas from 40 to 500 °C.

Atomic force microscopy

Roughness. in order to characterize and compare the surface textures of GLNs, the arithmetic average roughness (R_a) was extracted from raw AFM height images. R_a is frequently used for nanoscale systems because of its simple physical interpretation, especially for relatively homogeneous surfaces like nanoparticles. R_a is the mean of the absolute deviations of height values from the mean plane. While root mean square (RMS) roughness R_{RMS} is more sensitive to extreme height variations, R_a provides a reliable metric for comparative analysis when the goal is to assess overall surface irregularity rather than isolated asperities, as supported by previous AFM-based nanoparticle and thin-film studies.[62] The surface roughness was quantified as the arithmetic mean of the absolute height deviations from the mean surface plane as follows:

$$R_a = \frac{1}{N} \sum_{j=1}^{N} |Z_j|$$

where Z_j represents the vertical height deviation of each data point from the mean surface plane and N is the total number of sampled points within the selected analysis area.

The observed variations in R_a indicate that the 0% GLNs exhibited an average roughness of 2.2 ± 0.7 nm, while the 0.001% GLNs showed a slightly higher roughness of 2.7 ± 0.7 nm. In contrast, the 0.01% GLNs demonstrated the highest surface roughness, with an R_a value of 3.2 ± 0.9 nm. Such differences in nanoscale roughness could result from the influence between particles, the process of adsorption, or the mechanics of interfacial contact.

High-resolution imaging. atomic force microscopy (AFM) (Bruker BioScope Resolve system, integrated with a NanoScope V controller) was used in peak force quantitative nanomechanics (PF-QNM) experimental mode. This method provides precise mechanical mapping and high-resolution surface topography at the same time. A SCANASYST-FLUID probe with a 20 nm tip radius and a spring constant between 0.5 and 0.7 N m^{-1} was used in the system. The NPs were accurately preserved throughout imaging by using a constant scan rate of 0.561 Hz, which had been incubated on glass slides overnight. The scan sizes were usually between 1 and 4 µm in order to fully cover various areas of interest. A consistent peak force of 750 pN was used to avoid any unintentional damage to the nanoparticles (NPs). In order to maximize the visualization while maintaining the integrity of the samples, the imaging resolution was set at 256 pixels per line. Clarity and high-fidelity data capture were ensured by maintaining the peak force amplitude and frequency at 250 nm and 1 kHz, respectively. To reduce environmental disruptions like thermal drift and mechanical vibrations, the system was kept in a temperature-controlled chamber, and all experiments were conducted in a liquid medium.

Data processing and analysis. following imaging, the acquired data underwent detailed analysis using Bruker's Nanoscope Analysis software. Structural attributes such as particle size ($N = 120$), shape, and topographical details ($N = 180$) were extracted from the spm height sensor images that provided quantitative data on the dimensions of the NPs. AFM topography images were acquired under identical scanning conditions to minimize measurement artifacts arising from scan size, pixel resolution, and tip-sample convolution effects, all of which are known to influence roughness values. In order to avoid edge effects and substrate contributions, roughness analysis was carried out on carefully chosen regions of interest that were big enough to capture representative surface features of the nanoparticles. Multiple randomly 180 GLNs were analyzed and the analysis area for a single particle was 70 nm × 70 nm. The roughness values were calculated directly from unfiltered height data to ensure that the extracted parameters represent intrinsic surface features rather than artifacts brought about by digital filtering.

Additionally, Young's modulus was analyzed from .pfc files that were obtained during peak force QNM mode imaging. Force–distance curves were collected for randomly selected NPs under identical loading conditions to minimize tip- and sample-dependent variability. Two contact mechanics models were used to extract Young's modulus (E) from the force-

indentation data (Fig. S11a): the Hertz model (Fig. S11b) ($n \sim 150$) and the cone–sphere model (Fig. S11c) ($n \sim 185$). These models utilize the interaction of the AFM probe with a compliant substrate to calculate Young's modulus of the NPs.

The Hertz model[63] describes the elastic indentation of a rigid spherical probe into an isotropic, homogeneous, and linearly elastic half-space. This approach is commonly used for shallow indentation depths where the AFM tip–NP interaction is dominated by purely elastic deformation. The governing force–indentation relationship is:

$$F = \frac{4}{3} \times \frac{E}{1 - \nu^2} \times \sqrt{R} \delta^{\frac{3}{2}} \qquad (1)$$

where ν is the Poisson's ratio, δ is the indentation depth, R is the indenter's radius, F is the indentation force, and E is Young's modulus.

The Hertz model was fit to force curves up to $\sim 10\%$ of the particle height, ensuring the validity of the small-deformation assumption. The Hertz model is particularly appropriate in regimes where the spherical tip apex dominates the contact geometry and deformations remain relatively shallow. On the other hand, the cone–sphere model[64] was applied to capture indentation regimes where conical contributions of the AFM tip become significant. This model accounts for both spherical and conical contact contributions depending on the ratio of the contact radius a to the spherical tip radius b. If $a \leq b$, then spherical contact dominates, reducing the relationship to the Hertzian form (eqn (1)). However, both conical and spherical components contribute to the contact if $a > b$, and the force is given by:

$$F = 2\frac{E}{1-\nu^2}\left[a\delta - \frac{a^2}{2\tan\theta}\left(\frac{\pi}{2} - a\sin\theta\left(\frac{b}{a}\right)\right) \\ - \frac{a^3}{3R} + (a^2 - b^2)^{\frac{1}{2}}\left(\frac{b}{2\tan\theta} + \frac{(a^2 - b^2)}{3R}\right)\right] \qquad (2)$$

where ν is the sample-dependent Poisson's ratio (usually between 0.2 and 0.5), δ is the indentation depth, F is the indentation force, E is Young's modulus, R is the indenter's radius, θ is the semi-apex angle of the conical portion of the tip, a is the contact radius, and b is the transition radius between spherical and conical contact regions. This model considers how the respective magnitudes of a and b determine the transition between spherical and conical interactions.

This dual-regime model is particularly suited for bi- or multi-layered NPs, as deformation may transition from spherical-dominated (elastic particle compression) to cone-dominated (bilayer bending and partial yielding) with increasing indentation. All force–indentation curves were fitted using nonlinear least-squares regression in Nanoscope Analysis (Bruker). Curves exhibiting adhesion instabilities, noise artifacts, or poor convergence ($R^2 < 0.90$) were excluded. The mean of Young's modulus was reported for each NP population. The cone–sphere model-derived moduli were presented in the main text, while comparisons between Hertz and cone–sphere models are shown in Table S3.

Inductively coupled plasma mass spectrometry. After preparation of GLNs, the optical density (O.D.) was checked, and different volumes of GLNs corresponding to O.Ds were weighed to obtain the corresponding weight. The GLNs were further digested with freshly prepared aqua regia (HCl : HNO$_3$, 3 : 1 v/v). The gold concentration was quantified by inductively coupled plasma mass spectrometry (ICP-MS) using an Agilent 7700 series instrument. Following digestion, the samples were diluted in an acidic matrix to fall within the instrument's linear dynamic range. The results obtained (ppb) were used to calculate the concentrations of Au (μg mL^{-1}) in different GLNs and used for further studies.

Cellular viability, intracellular uptake, and uptake inhibition analysis. *In vitro* cell viability of gold liposome nanohybrids was evaluated in MODE-K mouse gut epithelial cells and DC2.4 dendritic cell lines. Briefly, 5×10^3 cells per well were seeded into a 96-well plate and incubated overnight at 37 °C and 5% CO$_2$. Afterward, the medium was aspirated, and different GLNs (0%, 0.001% and 0.01%) were added into MODE-K and DC2.4 cells making the final concentrations indicated in Fig. S15. After incubation for 24 h, the cell viability was determined using CCK-8 assay as per the manufacturer's protocol.

For investigating the optimum concentration of GLNs for the visualization and quantification of the intracellular uptake, MODE-K cells and DC 2.4 cells (3×10^4 cells per well) were seeded in a Lab-Tek Chamber Slide and incubated at 37 °C and 5% CO$_2$. After overnight incubation, the medium was removed, and 0.001% GLNs equivalent to 2.5–15 μg mL^{-1} Au were added to the wells and further incubated for 6 h. After the incubation, the samples were removed, and the cells were washed with DPBS, fixed with 4% paraformaldehyde, and mounted with a coverslip. The slides were analyzed using the upright mode of an Echo Revolve microscope. The multiple-point cellular uptake study was also performed using the same method but using a fixed concentration of 5 μg mL^{-1} for all three GLNs. After incubating the cells for different time points (1–24 h) at 37 °C and 5% CO$_2$, the samples were removed, and the cells were washed, fixed and mounted with a coverslip followed by imaging. For the ICP-MS analysis, the cells were seeded in 24 well plates, incubated overnight followed by the addition of 5 μg mL^{-1} GLNs. After each time interval, the cells were collected centrifuged and the pellets were digested using aqua regia followed by the analysis as described above.

For the TEM analysis of cells, the cells were seeded on 12 mm RBS35 cleaned and UV sterilized coverslips in a 24 well plate followed by the addition of 0.01% GLNs. After the incubation, the cells were fixed with 1% paraformaldehyde and 3% glutaraldehyde in 0.1 M sodium cacodylate buffer, pH 7.2 at 4 °C. Samples were washed in cacodylate buffer and post-fixed with 1% osmium tetroxide in 0.1 M sodium cacodylate buffer for 1 hour at room temperature. Samples were washed with deionized water and *en bloc* stained using 2% uranyl acetate in distilled water for 1 hour. Samples were washed in distilled water dehydrated through a graded ethanol series (25, 50, 70, 85, 95, and 100%) for 1 hour each step.

Communication

Samples were further dehydrated with pure acetone and infiltrated with EmBed 812 formula (hard) for EPON epoxy resin (Electron Microscopy Sciences, Hatfield PA) with graded ratios of resin to acetone until fully infiltrated with pure epoxy resin (3 : 1, 1 : 1, 1 : 3, and pure) for 6–12 hours per step. Coverslips with cells were inverted and placed onto upright resin filled Beem capsules and polymerized at 70 °C for 48 h. Thick sections (1.5 μm) were made after removal of the coverslip using a Leica UC6 ultramicrotome (Leica Microsystems, Buffalo Grove, IL) and stained with Toluidine Blue-O. Thin sections were made at 60 nm and collected onto carbon film grids and post-stained with lead citrate to enhance contrast. TEM images were collected using a 200 kV JEOL JSM 2100 scanning transmission electron microscope (Japan Electron Optics Laboratories, USA, Peabody, MA) with a GATAN One View 4 K camera (Gatan Inc., Pleasanton, CA).

For cellular uptake inhibition studies, the cells were pre-incubated with different inhibitors including cytochalasin B (10 μg mL^{-1}, 2 h) for phagocytosis, genistein (200 μm, 1 h) for caveolae-mediated endocytosis, rottlerin (2 μm, 30 min) for macropinocytosis, and monodansyl cadaverine (200 μm, 10 min) for clathrin mediated endocytosis followed by the addition of GLNs equivalent to 5 μg mL^{-1} for 6 h. The cells were washed, fixed and counter-stained with 4′,6-diamidino-2-phenylindole (DAPI). Fluorescence microscopy with a trans and/or DAPI filter was used for visualizing the dark contrast of gold liposome nanohybrids in the cells. For the quantification of cell uptake/inhibition, 30 cells per sample were selected from multiple images of two different experiments using ImageJ software and averaged. Images underwent background subtraction and contrast enhancement followed by particle count from each cell. Prior to the inhibition studies, the cell viability of the cells treated with different inhibitors was also determined both in DC2.4 and MODE-K cells using CCK assay.

Live/dead assay. Live/dead assay was performed using calcein–AM and propidium iodide (PI) staining in both MODE-K and DC2.4 cells after photothermal therapy to determine the therapeutic efficacy of GLNs. Briefly, 5×10^4 cells per well were seeded into a 24-well plate and incubated overnight at 37 °C and 5% CO$_2$. The cells were then incubated with two different concentrations (10 μg mL^{-1} and 15 μg mL^{-1}) of GLNs (0%, 0.001% and 0.01%) for two different time points (6 h and 8 h). After the incubation, samples from each well were replaced with fresh media followed by exposure to 808 nm laser PSU-III-LED, (CNI Optoelectronics Technology Co., Ltd) at 1 W cm^{-2} for 5 min. The cells were further incubated for 24 h. The supernatants were collected and centrifuged to remove any cell debris and stored at −80 °C until further use. The cells were incubated with serum free media containing calcein (3 μM) and PI (1 μM) for 30 min at 37 °C. The cells were replaced with fresh Hanks buffered salt solution and imaged using fluorescence microscopy. The mean fluorescence intensity (MFI) of PI was calculated from multiple images using ImageJ software and averaged.

Enzyme-linked immunosorbent assay (ELISA). Cytokine analysis was performed using the cell supernatant collected after photothermal therapy for TNF-α (Thermo Fisher Scientific, cat# 88-7324-88) and IL12-p70 (Thermo Fisher Scientific, cat#88-7121-88) using an uncoated ELISA Kit according to the manufacturer's protocol. The ELISA concentrations were all normalized to their corresponding total protein concentrations using a BCA protein assay kit.

Seahorse XF extracellular flux analysis. The Seahorse XF extracellular flux analyzer provides a robust platform for real-time measurement of the extracellular acidification rate (ECAR), enabling the detailed characterization of metabolic pathways and the identification of potential therapeutic targets. The ECAR of MODE-K cells was measured using a Seahorse XFe24 Extracellular Flux Analyzer (Agilent Technologies, Santa Clara, CA) following the manufacturer's protocol described for the Glycolysis Stress Test Kit (Agilent Technologies, Santa Clara, CA), respectively. In short, MODE-K cells were cultured in a 24-well Seahorse plate (40×10^3 cells per well) overnight. The following day, the cells were incubated with 10 μg mL^{-1} GLNs for 7–8 h. After the incubation period, the culture medium was replaced with fresh medium, and the samples were subsequently exposed to 808 nm laser irradiation at 1 W cm^{-2} for 5 min. The next day, the cells were washed with Seahorse XF Base Medium (Agilent Technologies), supplemented with 2 mM L-glutamine (pH 7.4) and incubated in assay medium for 1 h in a non-CO$_2$ incubator at 37 °C. The sensor plate was then filled with the modulator compounds and loaded onto the machine, followed by the cell plate. The flux measurements were initially recorded under basal conditions, followed by the sequential addition of modulators glucose (10 mM), oligomycin (1 μM), and 2-deoxy-glucose (2-DG) (50 mM) for ECAR measurement. The resultant data were analyzed using the Seahorse Analytics program (Agilent Technologies), and the ECAR values were normalized to their corresponding total protein concentrations, as measured using a BCA protein assay kit.

Statistical analysis

The outcomes are expressed as mean ± standard deviation and all statistical analysis was performed via ANOVA using Graph-Pad Prism Software (San Diego, CA). Here, * represents a p value <0.05, ** represents a p value <0.01 and, *** represents a p value <0.001 and ns stands for not significant.

Author contributions

RB conceived the project idea, directed the study design, and edited the manuscript. APM and VK performed the data interpretation, data analysis and wrote the manuscript. NM performed AFM experiments and data interpretation and wrote part of the Methods section. AS provided insights into AFM measurement and analysis and edited the manuscript. SHP and WH helped with the ICP-MS analysis. SKN and SKM performed and analyzed the Seahorse assay. SU trained APM and VK in liposome preparation and initial experiments. XW helped with optimization of chitosan coating methods.

Conflicts of interest

There are no conflicts to declare. SKM holds a financial interest in ImmunoNanoMed. All other authors declare no competing financial interest.

Data availability

The data supporting this article have been included as part of the supplementary information (SI). Supplementary information: photothermal efficiency of GLNs developed with DPPC/DSPE-PEG/DSPE-PEG-Amine liposomes and DPPC/DSPE-PEG liposomes; physicochemical characterization of GLNs developed with DPPC/Chol liposomes and 0.1% and 0.3% of chitosan coating, and representative TEM images of DPPC/Chol bare liposome and chitosan-coated liposome; lower magnification TEM images of GLNs developed with DPPC/Chol liposomes and 0%, 0.001%, and 0.01% chitosan; EDS analysis of 0% GLNs; EDS analysis of 0.001% GLNs; EDS analysis of 0.01% GLNs; physicochemical characterization of DPPC/Chol liposome with different concentrations of 0.001%, 0.01%, 0.1%, and 0.3% of chitosan coating; physicochemical characterization of DPPC/Chol/DSPE-PEG liposome with different concentrations of 0.001%, 0.01%, 0.1%, and 0.3% of chitosan coating; physicochemical characterization of GLNs developed with DPPC/Chol/DSPE-PEG liposome with different concentrations of 0.001%, 0.01%, 0.1% and 0.3% of chitosan coating; normalized Raman intensity of the liposome alone; thermogravimetry analysis of liposomes and GLNs; *in vitro* stability of the GLNs 0%, 0.001% and 0.01%; contact mechanics model used to extract the Young's modulus from the force-indentation data, the Hertz model, and the Cone-Sphere model; Young's modulus measured for the different samples using the Hertz model; Young's modulus of bulk/metal NPs; Reference on cell studies done with NPs and substrate stiffness; Quantitative comparison of nanoparticle size and Young's Modulus estimations using Hertz and Cone-Sphere Contact Mechanics; *in vitro* cellular viability of finalized GLNs developed with DPPC/choleserol liposomes with (0.001% and 0.01%) or without chitosan (0%) in DC 2.4 and MODE-K cells; *in vitro* cell uptake of different concentrations of finalized GLNs developed with DPPC/cholesterol liposomes and 0.001% chitosan in DC2.4 and MODE-K cells; *in vitro* cell uptake of finalized GLNs developed with DPPC/cholesterol liposomes with (0.001% and 0.01%) or without chitosan (0%) in DC 2.4 and MODE-K cells; *in vitro* cell uptake of different GLNs at different time points from 1 h to 24 h in DC2.4 and MODE-K cells validated using ICP-MS analysis; *in vitro* cell viability performed after treating DC2.4 and MODE-K cells with different inhibitors. Representative overlay images of DC2.4 and MODE-K cells incubated with GLNs for 6 h with and without pre-treatment with genistein; representative images of MODE-K and DC2.4 cells from live/dead assay; quantification of the different functional parameters for glycolysis from ECAR curves: (a) glycolysis and (b) glycolytic reserve. See DOI: https://doi.org/10.1039/d5mh02229k.

Acknowledgements

References

1 M. Wang, R. Sun, H. Chen, T. Yoshitomi, H. Mamiya, M. Takeguchi, N. Kawazoe, Y. Yang and G. Chen, *Mater. Horiz.*, 2025, **12**, 4363–4378.

2 S. Behzadi, V. Serpooshan, W. Tao, M. A. Hamaly, M. Y. Alkawareek, E. C. Dreaden, D. Brown, A. M. Alkilany, O. C. Farokhzad and M. Mahmoudi, *Chem. Soc. Rev.*, 2017, **46**, 4218–4244.

3 M. Sousa de Almeida, E. Susnik, B. Drasler, P. Taladriz-Blanco, A. Petri-Fink and B. Rothen-Rutishauser, *Chem. Soc. Rev.*, 2021, **50**, 5397–5434.

4 J. J. Rennick, A. P. R. Johnston and R. G. Parton, *Nat. Nanotechnol.*, 2021, **16**, 266–276.

5 V. T. Cong, J. L. Houng, M. Kavallaris, X. Chen, R. D. Tilley and J. J. Gooding, *Chem. Soc. Rev.*, 2022, **51**, 7531–7559.

6 A. K. Rengan, A. B. Bukhari, A. Pradhan, R. Malhotra, R. Banerjee, R. Srivastava and A. De, *Nano Lett.*, 2015, **15**, 842–848.

7 Y.-C. Chen, L.-C. Chang, Y.-L. Liu, M.-C. Chang, Y.-F. Liu, P.-Y. Chang, D. Manoharan, W.-J. Wang, J.-S. Chen, H.-C. Wang, W.-T. Chiu, W.-P. Li, H.-S. Sheu, W.-P. Su and C.-S. Yeh, *Nat. Commun.*, 2025, **16**, 3253.

8 U. Patel, K. Rathnayake, N. Singh and E. C. Hunt, *ACS Appl. Bio Mater.*, 2023, **6**, 1915–1933.

9 Y.-C. Ou, J. A. Webb, S. Faley, D. Shae, E. M. Talbert, S. Lin, C. C. Cutright, J. T. Wilson, L. M. Bellan and R. Bardhan, *ACS Omega*, 2016, **1**, 234–243.

10 T. K. Sau, A. S. Urban, S. K. Dondapati, M. Fedoruk, M. R. Horton, A. L. Rogach, F. D. Stefani, J. O. Rädler and J. Feldmann, *Colloids Surf., A*, 2009, **342**, 92–96.

11 S.-H. Park, S.-G. Oh, J.-Y. Mun and S.-S. Han, *Colloids Surf., B*, 2006, **48**, 112–118.

12 M. Mathiyazhakan, Y. Yang, Y. Liu, C. Zhu, Q. Liu, C. D. Ohl, K. C. Tam, Y. Gao and C. Xu, *Colloids Surf., B*, 2015, **126**, 569–574.

13 F. Xu, A. Bandara, H. Akiyama, B. Eshaghi, D. Stelter, T. Keyes, J. E. Straub, S. Gummuluru and B. M. Reinhard, *Proc. Natl. Acad. Sci. U. S. A.*, 2018, **115**, E9041–E9050.

14 Y. Hui, D. Wibowo, Y. Liu, R. Ran, H.-F. Wang, A. Seth, A. P. J. Middelberg and C.-X. Zhao, *ACS Nano*, 2018, **12**, 2846–2857.

15 D. Zou, Z. Wu, X. Yi, Y. Hui, G. Yang, Y. Liu, H. Wang, A. Brooks, H. Wang, X. Liu, Z. P. Xu, M. S. Roberts, H. Gao and C.-X. Zhao, *Proc. Natl. Acad. Sci. U. S. A.*, 2023, **120**, e2214757120.

16 A. C. Anselmo and S. Mitragotri, *Adv. Drug Delivery Rev.*, 2017, **108**, 51–67.

17 L. Zheng, S. R. Bandara, Z. Tan and C. Leal, *Proc. Natl. Acad. Sci. U. S. A.*, 2023, **120**, e2301067120.

18 D. Tang, W. Fan, M. Xiong, M. Li, B. Xiong and X.-B. Zhang, *Anal. Chem.*, 2021, **93**, 17036–17042.

19 A. Lesniak, A. Salvati, M. J. Santos-Martinez, M. W. Radomski, K. A. Dawson and C. Åberg, *J. Am. Chem. Soc.*, 2013, **135**, 1438–1444.

20 Y. Bai, H. Xing, P. Wu, X. Feng, K. Hwang, J. M. Lee, X. Y. Phang, Y. Lu and S. C. Zimmerman, *ACS Nano*, 2015, **9**, 10227–10236.

21 P. Gurnani, C. Sanchez-Cano, H. Xandri-Monje, J. Zhang, S. H. Ellacott, E. D. H. Mansfield, M. Hartlieb, R. Dallmann and S. Perrier, *Small*, 2022, **18**, 2203070.

22 Y. Sung, Y. Choi, E. S. Kim, J. H. Ryu and I. C. Kwon, *J. Controlled Release*, 2025, **380**, 524–538.

23 Y.-Q. Chen, M.-D. Xue, J.-L. Li, D. Huo, H.-M. Ding and Y. Ma, *ACS Nano*, 2024, **18**, 6463–6476.

24 H. Lee, D. Vanhecke, S. Balog, P. Taladriz-Blanco, A. Petri-Fink and B. Rothen-Rutishauser, *Nanoscale Adv.*, 2024, **6**, 4572–4582.

25 S. A. MacParland, K. M. Tsoi, B. Ouyang, X.-Z. Ma, J. Manuel, A. Fawaz, M. A. Ostrowski, B. A. Alman, A. Zilman, W. C. W. Chan and I. D. McGilvray, *ACS Nano*, 2017, **11**, 2428–2443.

26 Y. Hui, X. Yi, D. Wibowo, G. Yang, A. P. J. Middelberg, H. Gao and C.-X. Zhao, *Sci. Adv.*, 2020, **6**, eaaz4316.

27 H. Hinterwirth, S. Kappel, T. Waitz, T. Prohaska, W. Lindner and M. Lämmerhofer, *ACS Nano*, 2013, **7**, 1129–1136.

28 A. J. Mieszawska, W. J. M. Mulder, Z. A. Fayad and D. P. Cormode, *Mol. Pharmaceutics*, 2013, **10**, 831–847.

29 A. K. Rengan, M. Jagtap, A. De, R. Banerjee and R. Srivastava, *Nanoscale*, 2014, **6**, 916–923.

30 Y. Lyu, L. M. Becerril, M. Vanzan, S. Corni, M. Cattelan, G. Granozzi, M. Frasconi, P. Rajak, P. Banerjee, R. Ciancio, F. Mancin and P. Scrimin, *Adv. Mater.*, 2024, **36**, 2211624.

31 L. Malassis, R. Dreyfus, R. J. Murphy, L. A. Hough, B. Donnio and C. B. Murray, *RSC Adv.*, 2016, **6**, 33092–33100.

32 L. Luo, Y. Bian, Y. Liu, X. Zhang, M. Wang, S. Xing, L. Li and D. Gao, *Small*, 2016, **12**, 4103–4112.

33 J. Qiu, M. Xie, T. Wu, D. Qin and Y. Xia, *Chem. Sci.*, 2020, **11**, 12955–12973.

34 R. Hao, M. Jiao, X. Xu, D. Wu, H. Wei and L. Zeng, *J. Mater. Chem. B*, 2025, **13**, 2042–2051.

35 K. Czamara, K. Majzner, M. Z. Pacia, K. Kochan, A. Kaczor and M. Baranska, *J. Raman Spectrosc.*, 2015, **46**, 4–20.

36 C. Ou, S. Li, J. Shao, T. Fu, Y. Liu, W. Fan, X. Yang and X. Bi, *Cogent Chem.*, 2016, **2**, 1216247.

37 S. M. Kong, D. F. Costa, A. Jagielska, K. J. Van Vliet and P. T. Hammond, *Proc. Natl. Acad. Sci. U. S. A.*, 2021, **118**, e2104826118.

38 J. L. Voigt, J. Timmer, F. Pennarola, J. Christian, N. Meng, J. W. Blumberg, U. S. Schwarz, D. Grimm and E. A. Cavalcanti-Adam, *Adv. Funct. Mater.*, 2024, **34**, 2304674.

39 A. Sarkar, *Front. Nanotechnol.*, 2022, 32021.

40 N. Masud, M. H. H. Hasib, B. Ibironke, C. Block, J. Hughes, A. Ekpenyong and A. Sarkar, *Sci. Rep.*, 2025, **15**, 19302.

41 P. Guo, D. Liu, K. Subramanyam, B. Wang, J. Yang, J. Huang, D. T. Auguste and M. A. Moses, *Nat. Commun.*, 2018, **9**, 130.

42 Y. Duan, Y. Liu, J. Li, H. Wang and S. Wen, *Polymers*, 2018, **10**, 383.

43 V. Dodane, M. Amin Khan and J. R. Merwin, *Int. J. Pharm.*, 1999, **182**, 21–32.

44 K. A. Beningo and Y.-L. Wang, *J. Cell Sci.*, 2002, **115**, 849–856.

45 R. Hartmann, M. Weidenbach, M. Neubauer, A. Fery and W. J. Parak, *Angew. Chem., Int. Ed.*, 2015, **54**, 1365–1368.

46 X. Wen, L. Ou, G. Cutshaw, S. Uthaman, Y.-C. Ou, T. Zhu, S. Szakas, B. Carney, J. Houghton, A. Gundlach-Graham, M. Rafat, K. Yang and R. Bardhan, *Small*, 2023, **19**, 2204293.

47 T. B. Gandek, L. van der Koog and A. Nagelkerke, *Adv. Healthcare Mater.*, 2023, **12**, 2300319.

48 X. Xie, J. Liao, X. Shao, Q. Li and Y. Lin, *Sci. Rep.*, 2017, **7**, 3827.

49 N. Aibani, R. Rai, P. Patel, G. Cuddihy and E. K. Wasan, *Pharmaceutics*, 2021, **13**, 1686.

50 J. Jia, Y. Zhang, Y. Xin, C. Jiang, B. Yan and S. Zhai, *Front. Oncol.*, 2018, **8**, 404.

51 G. Matsumoto, T. Ueda, J. Shimoyama, H. Ijiri, Y. Omi, H. Yube, Y. Sugita, K. Kubo, H. Maeda, Y. Kinoshita, D. G. Arias, J. Shimabukuro, E. Kotani, S. Kawamata and H. Mori, *Sci. Rep.*, 2012, **2**, 935.

52 J. Rejman, V. Oberle, I. S. Zuhorn and D. Hoekstra, *Biochem. J.*, 2004, **377**, 159–169.

53 M. Ghattas, G. Dwivedi, A. Chevrier, D. Horn-Bourque, M. G. Alameh and M. Lavertu, *RSC Adv.*, 2025, **15**, 896–909.

54 A. P. Mathew, S. Uthaman, I. Antony, S. Kothadiya, L. Liu, B. Narasimhan and R. Bardhan, *ACS Appl. Mater. Interfaces*, 2025, **17**, 37806–37825.

55 G. P. Cutshaw, S. Kothadiya, S. Uthaman, D. N. Pandya, X. Wen, A. Mathew, A. Sinha, I. Antony, A. E. Vilgelm, T. J. Wadas, J. S. Mitchell and R. Bardhan, *ACS Appl. Mater. Interfaces*, 2025, **17**, 59051–59066.

56 X. Zheng, T. Wang, J. Gong, P. Yang, Y. Zhang, Y. Zhang, N. Cao, K. Zhou, Y. Li, Y. Hua, D. Zhang, Z. Gu and Y. Li, *Mater. Horiz.*, 2024, **11**, 4998–5016.

57 L. Zhao, M. Hu, X. Yin, H. Yang, L. Zhu, P. Sun, X. Wang, S. Ai, Y. Zheng, G. Li, T. Yang, X. Chen and J. Zhang, *Mater. Horiz.*, 2025, **12**, 9679–9696.

58 S. Wang, J. Xin, L. Zhang, Y. Zhou, C. Yao, B. Wang, J. Wang and Z.-X. Zhang, *Int. J. Nanomed.*, 2018, **13**, 2143–2160.

59 K. Koga, T. Tagami and T. Ozeki, *Colloids Surf., A*, 2021, **626**, 127038.

60 M. Michael Dcona, Q. Yu, J. A. Capobianco and M. C. Hartman, *Chem. Commun.*, 2015, **51**, 8477–8479.

61 S. Biswas, N. S. Dodwadkar, R. R. Sawant and V. P. Torchilin, *Bioconjugate Chem.*, 2011, **22**, 2005–2013.

62 F. El Feninat, S. Elouatik, T. H. Ellis, E. Sacher and I. Stangel, *Appl. Surf. Sci.*, 2001, **183**, 205–215.

63 E. C. Faria, N. Ma, E. Gazi, P. Gardner, M. Brown, N. W. Clarke and R. D. Snook, *Analyst*, 2008, **133**, 1498–1500.

64 B. J. Briscoe, K. S. Sebastian and M. J. Adams, *J. Phys. D: Appl. Phys.*, 1994, **27**, 1156.